

## BIOCHEMISTRY

# Structure of the saxiphilin:saxitoxin (STX) complex reveals a convergent molecular recognition strategy for paralytic toxins

Tien-Jui Yen<sup>1</sup>, Marco Lolicato<sup>1</sup>, Rhiannon Thomas-Tran<sup>2\*</sup>, J. Du Bois<sup>2</sup>, Daniel L. Minor Jr.<sup>1,3,4,5,6†</sup>

Dinoflagelates and cyanobacteria produce saxitoxin (STX), a lethal bis-guanidinium neurotoxin causing paralytic shellfish poisoning. A number of metazoans have soluble STX-binding proteins that may prevent STX intoxication. However, their STX molecular recognition mechanisms remain unknown. Here, we present structures of saxiphilin (Sxph), a bullfrog high-affinity STX-binding protein, alone and bound to STX. The structures reveal a novel high-affinity STX-binding site built from a “proto-pocket” on a transferrin scaffold that also bears thyroglobulin domain protease inhibitor repeats. Comparison of Sxph and voltage-gated sodium channel STX-binding sites reveals a convergent toxin recognition strategy comprising a largely rigid binding site where acidic side chains and a cation- $\pi$  interaction engage STX. These studies reveal molecular rules for STX recognition, outline how a toxin-binding site can be built on a naïve scaffold, and open a path to developing protein sensors for environmental STX monitoring and new biologics for STX intoxication mitigation.

## INTRODUCTION

Saxitoxin (STX), a bis-guanidinium small molecule produced by brackish and freshwater cyanobacteria and oceanic dinoflagelates associated with red tides, is one of the most lethal neurotoxins, causes paralytic shellfish poisoning (PSP), and is the only marine toxin that is declared a chemical weapon (1, 2). Its toxicity is thought to arise primarily from inhibition of select voltage-gated sodium channel ( $\text{Na}_V$ ) isoforms (3), although STX may affect other channels (4, 5) and enzymes (6). PSP caused by STX represents a notable public health and commercial hazard that is an increasing problem due to climate change (7). Consequently, shellfish for human consumption are monitored globally for PSP toxins. Current STX detection methods use a cumbersome mouse viability assay (8). Thus, there is great interest in developing better analytical techniques for measuring STX and related congeners in food sources (7–9).

Nature uses diverse strategies to counter toxin exposure that include target protein resistance mutations, toxin sequestration, and toxin removal (10, 11). Although the best understood toxin resistance strategies involve target protein mutations (10, 12, 13), frogs display unusual resistance to STX poisoning (14, 15) that is not believed to involve altered responses of frog  $\text{Na}_V$ s to STX (16). Saxiphilin (Sxph), a 91-kDa transferrin homolog, is an STX-binding protein from American bullfrog (*Rana catesbeiana*) heart and plasma (16–20). This soluble, dual-function protein has a single high-affinity STX-binding site [ $K_d$  (dissociation constant),  $\sim 0.2$  nM] that recognizes certain STX derivatives (16, 21, 22) and has two  $\sim 60$  residue thyroglobulin type I (Thy1) repeats (18) that act as potent [ $K_i$  (inhibi-

tion constant),  $\sim 1$  nM] cysteine protease inhibitors (23). Other soluble STX-binding proteins have been identified in pufferfish (24, 25), cockles (26), and crabs (27), and STX-binding activity has been reported in the plasma, hemolymph, and tissues from arthropods (19), amphibians (28), fish (19), and reptiles (19). Hence, it is thought that Sxph and analogous toxin-binding proteins constitute a second, less well-characterized toxin resistance mechanism involving toxin sequestration (10, 16, 19).

Here, we present high-resolution x-ray crystal structures of apo-Sxph and STX-bound Sxph. These structures reveal key Sxph architectural features, how Sxph recognizes STX, and how the Thy1 domains may engage proteases. Remarkably, the two best-characterized high-affinity STX targets, Sxph and  $\text{Na}_V$ s (29), share a core molecular recognition motif that defines a fingerprint for STX molecular recognition. This information should serve as a touchstone for understanding how STX interacts with channels and other targets (6) and provide guidance for the design of new molecular sensors for STX and related toxins.

## RESULTS

### Sxph crystal structure reveals a modified transferrin fold

The 2.5-Å resolution x-ray crystal structure of American bullfrog (*R. catesbeiana*) Sxph (Fig. 1A, fig. S1, A and B, and table S1) revealed a bilobal organization similar to transferrins (30, 31), consisting of an N-lobe (residues 1 to 88 and 232 to 465) and a C-lobe (residues 470 to 825) connected by a linker. Both lobes contain two subdomains, designated N1 (residues 1 to 88 and 389 to 465), N2 (residues 232 to 388), C1 (residues 470 to 557 and 726 to 825), and C2 (residues 558 to 725). The N1 and C1 subdomains comprise discontinuous polypeptides into which N2 and C2 are inserted, respectively (fig. S2). Unlike other transferrin family members, Sxph has a 143-residue (residues 89 to 231) insertion between N1 and N2 that encodes two Thy1 repeats (fig. S2) (18, 23). The two Sxph protomers in the asymmetric unit are essentially identical except for a displacement of the first thyroglobulin repeat by  $\sim 24^\circ$  (fig. S1B). Hence, our description focuses on the more complete protomer B.

<sup>1</sup>Cardiovascular Research Institute, University of California, San Francisco, San Francisco, CA 94158, USA. <sup>2</sup>Department of Chemistry, Stanford University, Stanford, CA 94305, USA. <sup>3</sup>Departments of Biochemistry and Biophysics, and Cellular and Molecular Pharmacology, University of California, San Francisco, San Francisco, CA 94158, USA. <sup>4</sup>California Institute for Quantitative Biomedical Research, San Francisco, CA 94158, USA. <sup>5</sup>Kavli Institute for Fundamental Neuroscience, University of California, San Francisco, San Francisco, CA 94158, USA. <sup>6</sup>Molecular Biophysics and Integrated Bio-imaging Division, Lawrence Berkeley National Laboratory, Berkeley, CA 94720, USA.

\*Present address: Gilead Sciences, 333 Lakeside Drive, Foster City, CA 9440, USA.

†Corresponding author. Email: daniel.minor@ucsf.edu

The organization of the Sxph core architecture (N1, N2, C1, and C2) is conserved with transferrin (Fig. 1B). Sxph has 21 disulfides. Fourteen are conserved in the transferrin family. Seven are unique (Fig. 1C), of which five are in the Thy1 repeats (SS4 to SS8). The other two connect the  $\alpha$ 1N1 and  $\alpha$ 4N1 C-terminal ends (SS3) and the interdomain linker at the start of N2 to the C2 C-terminal tail (SS9) (Fig. 1C and fig. S2). The two Sxph lobes are related by a rigid body motion around the intersubdomain hinge that involves both a closure ( $\sim 30^\circ$ ) and a twist ( $\sim 60^\circ$ ) between the relatively closed (N-lobe) and open (C-lobe) conformations, respectively, (fig. S1C) that resembles the lobe conformations defined by apo- and  $\text{Fe}^{3+}$ -bound transferrin (32). Similar to other transferrin family structures, there is a small ( $558 \text{ \AA}^2$ ) mainly hydrophobic interface between N-lobe and C-lobe.

Consistent with the inability of Sxph to bind  $\text{Fe}^{3+}$  (18, 31), almost all of the residues in each lobe required to coordinate  $\text{Fe}^{3+}$  and an associated carbonate (33) differ substantially from the conserved transferrin ligands (Fig. 1B and fig. S3). There are also no interlobe  $\gamma$ -turns, a feature of all avian and mammalian transferrins that is thought to aid interlobe cleft opening for  $\text{Fe}^{3+}$  binding (32, 34). Together, the structural data establish that Sxph has a transferrin-like fold having numerous modifications and demonstrate why Sxph lacks the classic transferrin  $\text{Fe}^{3+}$ -binding function (35).

### Sxph Thy1 repeats resemble Thy1 protease inhibitors

The  $\sim 60$  residue thyroglobulin motif occurs in diverse proteins such as thyroglobulin, insulin-like growth factor-binding proteins, and the p41 invariant (Ii) chain involved in major histocompatibility

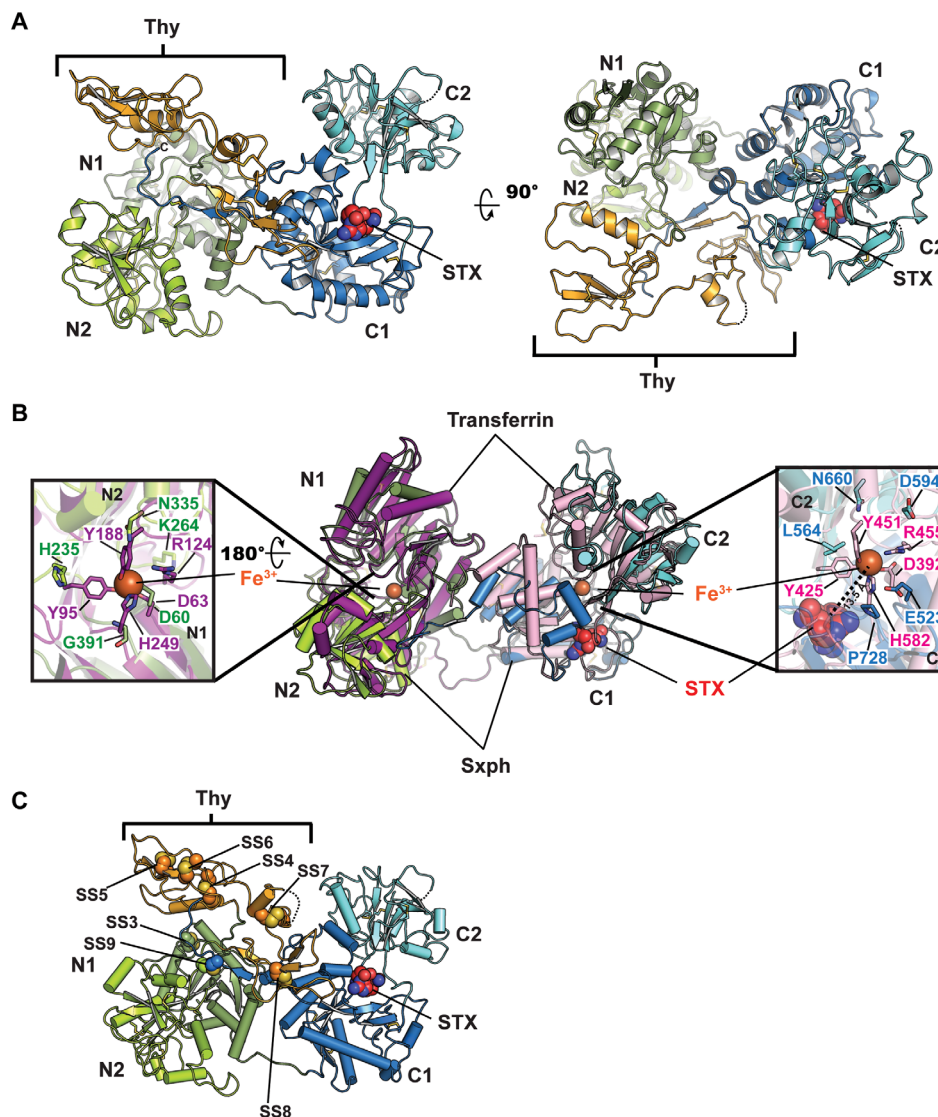


**Fig. 1. Sxph structure.** (A) *R. catesbeiana* Sxph:STX: complex ribbon diagram. Domains are indicated and are colored as follows: N1 (smudge), N2 (limon), thyroglobulin (Thy; bright orange), C1 (marine), and C2 (cyan). STX (red) is shown as space filling. (B) Superposition of Sxph and rabbit transferrin [Protein Data Bank (PDB): 1JNF] (32). Transferrin N-lobe and C-lobe are colored purple and pink, respectively. Sxph Thy1 repeats are not shown. Insets show transferrin  $\text{Fe}^{3+}$  ligands and Sxph equivalents as sticks. N domain: transferrin (purple) and Sxph (green); C domain: transferrin (pink) and Sxph (blue). STX (red) is shown as space filling. Right hand inset shows distance between the STX center and transferrin  $\text{Fe}^{3+}$ . (C) Cartoon diagram showing unique Sxph disulfide bonds in space filling representation: SS3 (Cys<sup>27</sup> to Cys<sup>417</sup>), SS4 (Cys<sup>91</sup> to Cys<sup>111</sup>), SS5 (Cys<sup>122</sup> to Cys<sup>129</sup>), SS6 (Cys<sup>131</sup> to Cys<sup>153</sup>), SS7 (Cys<sup>161</sup> to Cys<sup>183</sup>), SS8 (Cys<sup>203</sup> to Cys<sup>225</sup>), and SS9 (Cys<sup>234</sup> to Cys<sup>825</sup>). Colors and labels are the same as in (A).

complex class II maturation (36–39). The Sxph thyroglobulin domain forms an independent structure protruding from the N-lobe core (Fig. 1A). The two Thy1 repeats, Thy1-1 and Thy1-2 (Fig. 2A), adopt similar folds containing an  $\alpha$ -helix and two antiparallel  $\beta$ -strands. Thy1-1 conforms to the Thy1 type 1A motif stabilized by three disulfides (40), whereas Thy1-2 lacks the inter- $\beta$ -strand disulfide and conforms to the Thy1 type 1B motif (40). Both Sxph Thy1 repeats have a wedge shape presenting three loops from one end and bear strong structural similarity to each other and the p41 Ii Thy1 repeat (Fig. 2B) (38).

Similar to p41 Ii, Sxph is a potent cysteine protease inhibitor, affecting cathepsin L, cathepsin B, and papain with nanomolar potency (23). The two Thy1 repeats appear to enable Sxph to engage these targets with different stoichiometries (1:1 for cathepsin L and cathepsin B and 1:2 for papain) (23). Superposition of the p41:cathep-

sin L complex on the Thy1-1 and Thy1-2 domains (Fig. 2, C and D) indicates that the Thy1-1 repeat can bind the protease unhindered, whereas binding to Thy1-2 incurs clashes (Fig. 2D and fig. S4A). Superposition of papain, an enzyme very similar to cathepsin L but that Sxph binds with a 1:2 stoichiometry (23), shows similar clashes (fig. S4, A and B). Hence, it seems likely that local rearrangements mitigate these clashes. Comparison of the Sxph Thy1 domains with the p41:cathepsin L complex (38) highlights the features that likely contribute to Sxph Thy1 domain:protease interaction specificity (Fig. 2E). The conserved central Loop 2 (Fig. 2A) can be well positioned over the cathepsin L active site cysteine (Fig. 2E). Loop 3 of both repeats is longer than in p41 Ii (Fig. 2, A and B). However, this difference would not interfere with enzyme binding, as the p41 Loop 3 interactions between Arg<sup>250</sup> and the cathepsin L pocket lined by Trp<sup>189</sup> and Trp<sup>193</sup> are replaced by similar Sxph loop 3 tight turns in Thy1-1 and

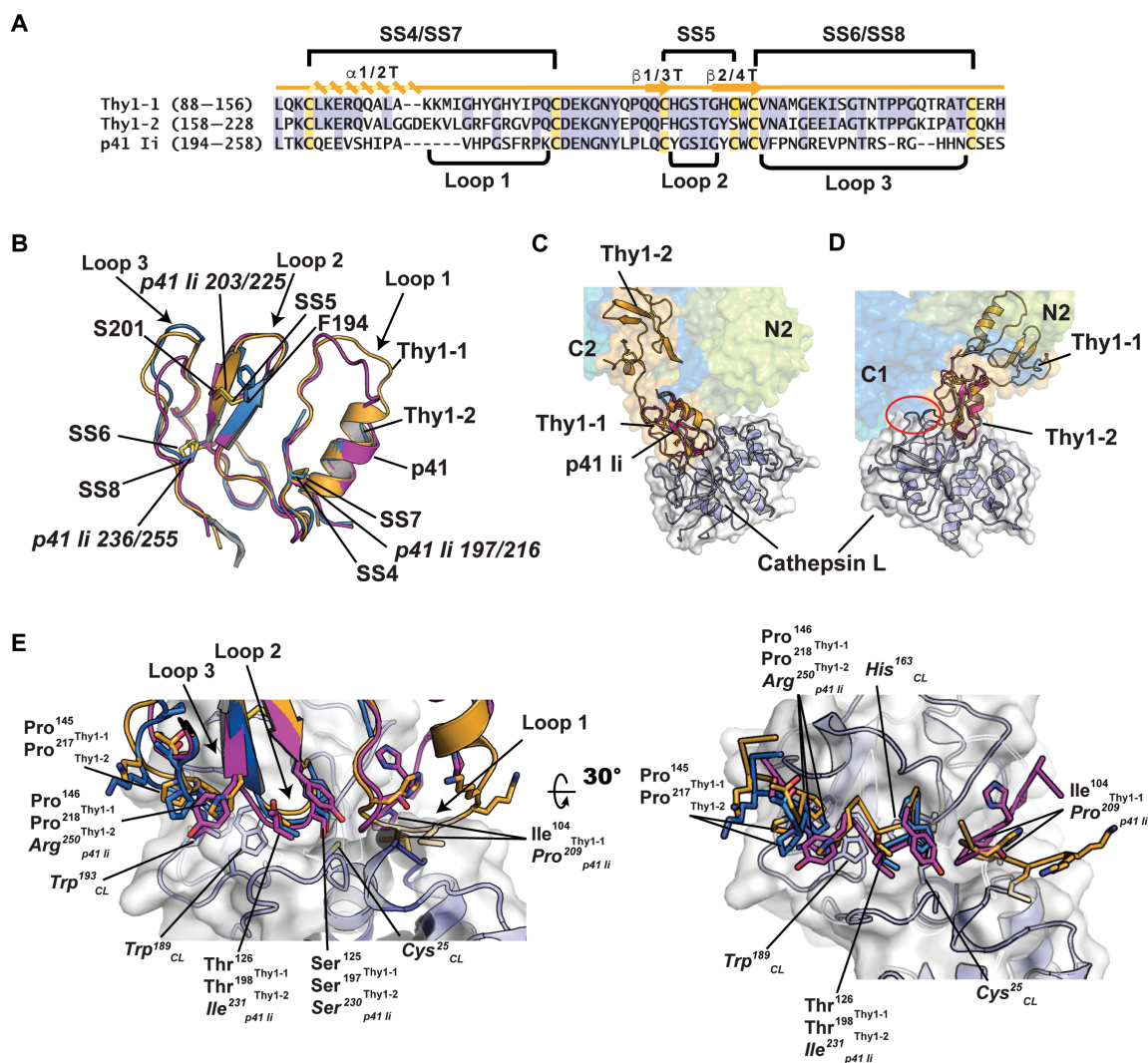


**Fig. 2. Comparison of Sxph Thy1-1 and Thy1-2 with p41 Ii.** (A) Sequence comparison. Thy1-1 and Thy1-2 secondary structure elements and disulfide bonds are indicated. Cysteines and conserved residues are highlighted yellow and blue, respectively. (B) Cartoon diagram superposition of Thy1-1 (light orange), Thy1-2 (marine), and p41 Ii (magenta) (PDB: 1ICF) (38). Disulfide bonds (italics) and select residues are labeled. Thy1-1 and Thy1-2 have root mean square deviation of C $\alpha$  position (RMSD<sub>C $\alpha$</sub> ) = 0.61 and 0.64 Å over 43 and 42 residues, respectively. p41 Ii has RMSD<sub>C $\alpha$</sub>  = 0.57 Å over 53 residues of Sxph Thy1-1 and Thy1-2. (C and D) Superposition of Sxph on the p41 Ii:cathepsin L complex (PDB: 1ICF) (38) using the (C) Thy1-1 and (D) Thy1-2 domains. In (D), red oval indicates cathepsin L and Sxph C1 clash. Sxph colors are the same as in Fig. 1A. (E) Superposition of Sxph Thy1-1 (light orange), Thy1-2 (marine), and p41 Ii (magenta) in the context of the p41 Ii:cathepsin L interface.

Thy1-2 (Fig. 2E). Loop 1 has the most varied conformations among Thy1 domains (fig. S4, C and D) and, in Thy1-1 and Thy1-2, has different mobilities, as Thy1-2 Loop 1 lacks visible electron density that indicates disorder. Comparison with the p41:cathepsin L complex shows that Thy1-1 Loop 1 occupies the protease S2 pocket in a manner in which any observed clashes could be relieved by modest reorganization. Loop 1, the point of highest sequence divergence between Thy1-1 and Thy1-2 (Fig. 2A), is likely responsible for binding specificity differences. Together, these analyses indicate how variations in Thy1 Loop 3 can recognize a common target, support the role of Loop 1 in protease recognition specificity (40), and suggest why Sxph binds similar proteases with different stoichiometries.

### Structure of the Sxph:STX complex reveals a novel STX-binding site

Sxph binds STX with high affinity ( $K_d$ , 0.2 nM) and a 1:1 stoichiometry (20). Crystals made by soaking apo-Sxph crystals with STX or by cocrystallization diffracted x-rays to 2.50- and 2.12-Å resolutions, respectively (table S1). The asymmetric units in both contained two essentially identical Sxph:STX complexes (root mean square deviation of C $\alpha$  position, 0.5 Å) that provide a high-resolution view of the Sxph:STX interaction (table S1). Because of its superior resolution and completeness, our description focuses on molecule B of the Sxph:STX cocrystallization complex.

Sxph and STX interact with a 1:1 stoichiometry matching biochemical studies (16, 21). However, contrary to the idea that the STX-binding site is made by a remodeled Fe<sup>3+</sup>-binding cavity in the C1-C2 Sxph interdomain cleft (20), the Sxph:STX structure shows that a novel, solvent-exposed surface C1 pocket of ~14 Å away from the C1-C2 cleft forms the STX-binding site (Fig. 1A and figs. S1A and S5A) comprising C1 domain elements  $\alpha$ 3C1,  $\beta$ 4C1,  $\alpha$ 6C1, and the  $\beta$ 6C1- $\alpha$ 6C1 loop (Fig. 3A). Counter to previous proposals (20, 22), there are no large-scale conformational changes between apo-Sxph and Sxph:STX (fig. S5A). Hence, the Sxph:STX interaction occurs in an entirely unanticipated manner.

STX binds the STX pocket in an orientation in which its five- and six-membered guanidinium rings engage the protein, while the C12 hydrated ketone and carbamoyl group point toward solvent (Fig. 3, A to C, and fig. S5B). The STX pocket uses a set of charged side chains that directly engage the toxin together with contributions from backbone hydrogen bonding groups, van der Waals interactions, and a cation- $\pi$  interaction (Fig. 3, A to C). A set of side chain carboxyls coordinate the five- and six-membered guanidinium rings engaging all available STX guanidinium nitrogen atoms. Asp<sup>785</sup> and Asp<sup>794</sup> form a network that encompasses the three nitrogen atoms of the guanidinium group on the five-membered ring (Fig. 3, A to C), whereas the Glu<sup>540</sup> side chain interacts with both available six-membered ring guanidinium nitrogens (Fig. 3, A to C). This intimate involvement of acidic side chains agrees with the observation that Sxph treatment with trimethylxonium tetrafluoroborate, a reagent that methylates aspartate and glutamate carboxylates, inhibits STX binding (20). Backbone carbonyl interactions from Asp<sup>785</sup> with the five-membered ring N16 atom and Tyr<sup>795</sup> with the six-membered ring N13 atom augment the side chain networks (Fig. 3C). Phe<sup>784</sup> forms the STX-binding pocket base and makes a cation- $\pi$  interaction with the STX five-membered ring guanidinium (Fig. 3, B and C). Thus, rather than hydrophobic interactions as proposed (22), multiple sets of complimentary charged-based interactions comprise the Sxph:STX complex.

Although there are no large-scale changes between apo-Sxph and Sxph:STX (fig. S5A), some local rearrangements in the STX-binding pocket are evident from the initial difference maps (fig. S1A) and structure refinement. Asp<sup>785</sup> shows the largest change and acts like a latch that faces away from the apo-Sxph pocket and that closes to interact with the STX N7 atom (Fig. 3, A and B, fig. S1A, and movie S1). The remaining changes involve a small movement of the Glu<sup>540</sup> away from the pocket and a ~15° rotation of the Tyr<sup>558</sup> ring (Fig. 3B and movie S1). Hence, Sxph:STX high-affinity interaction results from capture of the rigid toxin by an essentially preformed binding site.

Radioligand competitive displacement studies of STX derivatives (fig. S5B) (19) match the observed binding pose and side chain interactions. In line with the observation that STX carbamoyl moiety does not interact with Sxph, removal of this group (decarbamoyl STX; fig. S5B) or its modification with a sulfate (gonyautoxin V; fig. S5B) had only a ~2-fold and no impact on affinity, respectively (19). By contrast, hydroxylation of the six-membered ring N1 atom (neosaxitoxin; fig. S5B) reduced affinity by ~550-fold, supporting the importance of the interaction between N1 and Glu<sup>540</sup>. Further, sulfation of the C11 atom in the STX C1 derivative (fig. S5B) reduced binding relative to the STX B1 parent by ~150-fold, consistent with a clash between the sulfate and  $\alpha$ 6C1. The excellent agreement of these biochemical studies validates the observed binding pose and outlines how Sxph recognizes diverse naturally occurring STX derivatives.

### STX-binding site elements are absent from transferrins and Sxph N-lobe

Transferrins do not bind STX (35), and the STX-binding pocket resides in a region that has not been reported to bind small molecules in other transferrin family members. How then did nature sculpt the STX-binding pocket from a naïve transferrin scaffold? Comparison of Sxph with two exemplar transferrins, Fe<sup>3+</sup>-bound rabbit serum transferrin [Protein Data Bank (PDB): 1JNF] (41) (Fig. 4A) and apo-human serum transferrin (PDB: 2HAU) (32) (Fig. 4B), reveals a shallow “proto-pocket” on the transferrin C1 subdomain surface at the location of the STX-binding site. Notably, the structural homologs of the residues that form Sxph:STX interactions differ considerably (fig. S3). In the transferrins, positively charged and small hydrophobic residues are found at the positions of the Sxph acidic residues that coordinate the STX five-membered (Asp<sup>785</sup> and Asp<sup>794</sup>) and six-membered (Glu<sup>540</sup>) rings, respectively. Further, residues corresponding to Phe<sup>784</sup>, the amino acid responsible for the cation- $\pi$  interaction, are all branched, hydrophobic residues incapable of making this type of interaction.

Besides lacking the residues to coordinate STX, the rather shallow transferrin C1 proto-pocket is too small to accommodate a molecule the size of STX. Structural comparisons highlight changes in Sxph elements on opposite sides of the pocket that expand its size (Fig. 4, C to E). Namely, the Sxph  $\alpha$ 6C1 helix position differs from the corresponding transferrin helices (residues 643 to 648 and 646 to 650 in rabbit and human transferrin, respectively; Fig. 4, A and B), and the loop adjacent to the STX carbamate (residues 555 to 561) differs relative to the corresponding transferrin structure (residues 418 to 423 and 419 to 424 in rabbit and human transferrin, respectively; Fig. 4, A and B). This Sxph loop is buttressed by the  $\alpha$ 4C1 helix, which is absent in transferrin (Fig. 4, A and B, and fig. S3). Collectively, these changes create a site ringed by a set of negatively charged atoms that complement the dicationic STX (Fig. 4E).

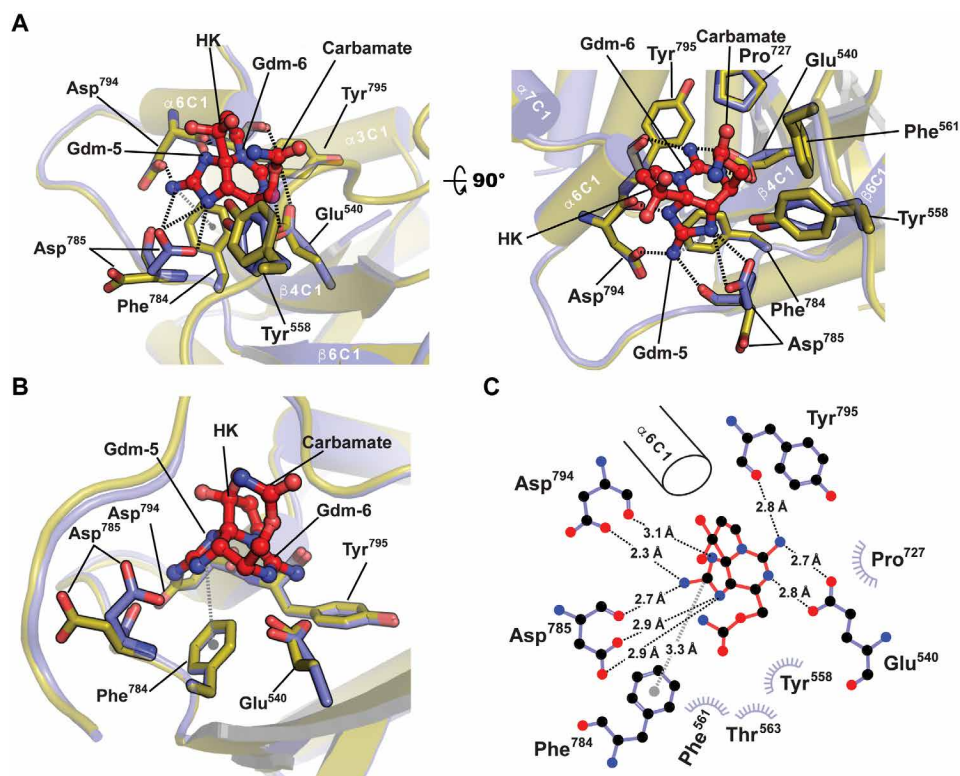


**Fig. 3. Sxph STX-binding site.** (A) Apo-Sxph (olive) and STX-bound Sxph (slate) superposition cartoon diagram. STX-interacting residues are shown as sticks. Key secondary structure elements are labeled. Black and gray dashed lines indicate hydrogen bond networks and the cation- $\pi$  interaction, respectively. STX is shown as red sticks. Gdm-5, Gdm-6, and HK indicate the five- and six-membered guanidinium rings and hemiketal, respectively. (B) STX-binding site highlighting the cation- $\pi$  interaction (gray) and Asp<sup>785</sup> movement. (C) LIGPLOT diagram of the STX-binding site.  $\alpha$ 6C1 is shown for orientation.

Sxph N1 and C1 are structurally similar (fig. S6A), and N1 has a proto-pocket that corresponds to the C1 STX-binding site. This proto-pocket is more open than in the transferrins and is framed on one side by two helices,  $\alpha$ 5N1 and  $\alpha$ 6N1, that match the C1 domain  $\alpha$ 6C1 and  $\alpha$ 7C1 (fig. S6B). However,  $\alpha$ 6N1 and Tyr<sup>82</sup> on the opposite side of the narrow N1 proto-pocket would clash with the toxin near the C12 hemiketal and C13 carbamate, respectively (fig. S6A). Most importantly, Sxph N1 lacks residues that could coordinate STX. The C1 residues that engage the two guanidinium rings, Glu<sup>540</sup>, Asp<sup>794</sup>, Asp<sup>785</sup>, and Phe<sup>784</sup>, are replaced in N1 by Ala<sup>79</sup>, Leu<sup>448</sup>, Ser<sup>441</sup>, and Leu<sup>440</sup>, respectively, rendering the site incapable of making the necessary electrostatic and cation- $\pi$  interactions (fig. S6A). Further, the N1 proto-pocket is occluded by  $\alpha$ 8C1,  $\beta$ 7C1, and  $\beta$ 5T (fig. S6C). Hence, a multitude of factors prevents Sxph from using the N1 sub-domain proto-pocket as a second STX-binding site.

### A frog Sxph homolog has the STX-binding motif

Although other STX-binding proteins have been reported (24–27), none are related to Sxph. We identified Sxph-like sequences in an invertebrate, springtail (*Folsomia candida*); two fish, Nile tilapia (*Oreochromis niloticus*) and Northern pike (*Esox lucius*); and the High Himalaya frog (*Nanorana parkeri*) (fig. S7). All share the transferrin fold core with Sxph and carry mutations that would prevent Fe<sup>3+</sup> binding. The springtail and High Himalaya frog sequences also have two Thy1 repeat insertions between the N1 and N2, making them closer homologs to Sxph than the fish sequences. Notably, the High

Himalaya frog sequence has the key features for STX recognition, namely, C1 equivalents of Glu<sup>540</sup>, Asp<sup>785</sup>, Asp<sup>794</sup>, and Phe<sup>784</sup> that match the STX recognition fingerprint. Hence, bullfrog Sxph is not unique and has a counterpart in a frog from a distantly related family (*Dicroglossidae*) that we name Sxph<sub>NP</sub>.

### Sxph and Nav<sub>s</sub> recognize STX using a similar molecular logic

Nav<sub>s</sub> are the primary target for the paralytic effects of STX and bind STX with nanomolar affinity, similar to Sxph (1, 20). To ask whether Nav<sub>s</sub> and Sxph use a common STX recognition strategy, we compared structures of the STX-binding sites of Sxph and the cockroach Nav<sub>V</sub>PaS:STX complex determined at 3.2-Å resolution by single-particle cryo-electron microscopy (cryo-EM; Fig. 5, A and B) (29). Although the two proteins are unrelated and some recognition details appear to differ, namely, at the site of the hydrated C12 ketone (29, 42, 43), there are remarkably common STX molecular recognition themes. The channel and Sxph both engage the five- and six-membered guanidinium rings using side chain carboxylates. Nav<sub>V</sub>PaS Glu<sup>378</sup> recognizes the five-membered ring similar to Sxph Asp<sup>794</sup>, and Nav<sub>V</sub>PaS Glu<sup>704</sup> coordinates the two available nitrogens of the six-membered guanidinium similar to Sxph Glu<sup>540</sup> (Fig. 5, C and D, and fig. S8A). Both glutamates are important for the Nav<sub>s</sub>:STX interaction (44, 45). The two proteins also use an aromatic ring to engage the STX concave face through a cation- $\pi$  interaction; however, the recognized STX ring differs. Nav<sub>V</sub>PaS Tyr<sup>376</sup>, a residue important for STX binding (45, 46), engages the STX six-membered ring, whereas Sxph Phe<sup>784</sup> interacts

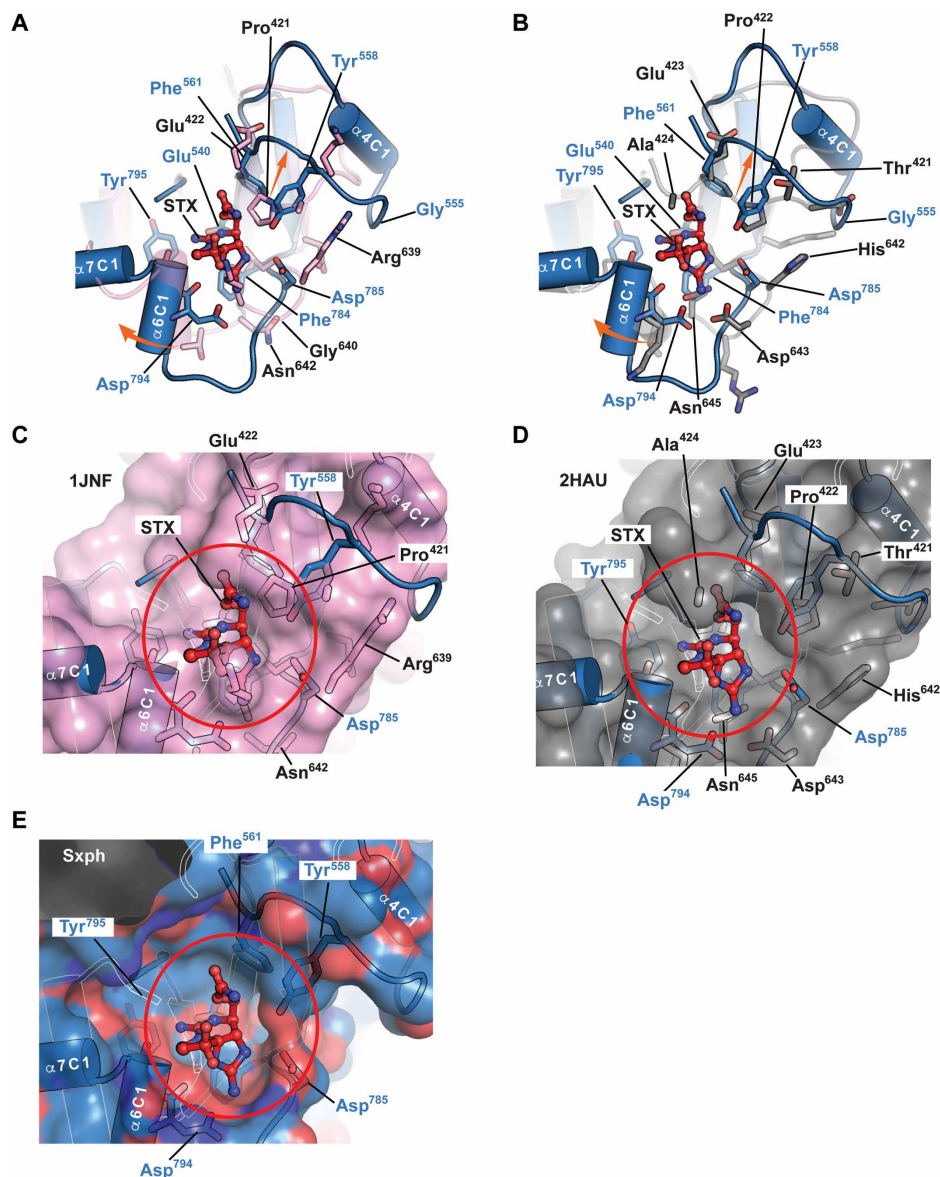


**Fig. 4. Sxph STX-binding site and transferrin proto-pocket.** (A and B) Superposition of the Sxph (marine) STX-binding site with (A) Fe<sup>3+</sup>-bound rabbit serum transferrin (PDB: 1JNF) (41) (pink) and (B) apo-human serum transferrin (PDB: 2HAU) (32) (gray). STX (red) is shown as sticks. Select residues are shown. Blue labels indicate Sxph residues. Orange arrows indicate changes between transferrin and Sxph. (C to E) Transferrin proto-pocket and Sxph STX-binding pocket comparisons. (C to E) show apo-transferrin (pink), transferrin (gray), and Sxph (marine) surfaces, respectively. In (C) and (D), labels indicate Sxph residues that break through the transferrin surface. Red circle highlights the STX-binding site. STX is shown as space filling. Sxph surface is colored by atom type, where red and blue denote oxygen and nitrogen, respectively.

with the five-membered ring (fig. S8B). Similar interactions are found in the recent 3.2-Å cryo-EM structure of a human Na<sub>v</sub>1.7:STX complex (Fig. 5E and fig. S8, B to D) (47). Although the resolutions of the Na<sub>v</sub>PaS:STX and Na<sub>v</sub>1.7:STX structures and issues regarding acidic side chain definition by cryo-EM relative to x-ray studies (48–50) place limits on a very detailed comparison of STX binding, it is obvious that the two completely unrelated proteins, Sxph and Na<sub>v</sub>s, share general STX recognition rules (Fig. 5E).

## DISCUSSION

The Sxph structure defines a paradigm for molecular recognition of STX, one of nature’s most lethal poisons (1, 3, 6) at atomic resolu-

tion. The Sxph core is built from the transferrin fold (Fig. 1B), a family of soluble proteins best known for Fe<sup>3+</sup> transport (30, 31), that has been modified to act as a “dual-function” protein that can make high-affinity interactions with STX and cysteine proteases. Contrary to expectations (20), the STX-binding site is not a remodeled version of the Fe<sup>3+</sup>-binding site but resides at a unique locale on the C1 domain. This high-affinity binding site undergoes minimal conformational changes upon binding the rigid STX scaffold. Remarkably, the general blueprint for STX recognition by Sxph using side chain carboxylates, a cation- $\pi$  interaction, and a largely rigid binding site is shared with Na<sub>v</sub>s (1, 13, 29, 44–47). This commonality between a 91-kDa soluble protein and a ~200-kDa membrane protein ion channel unmasks an extraordinary convergence of STX molecular recognition strategies.

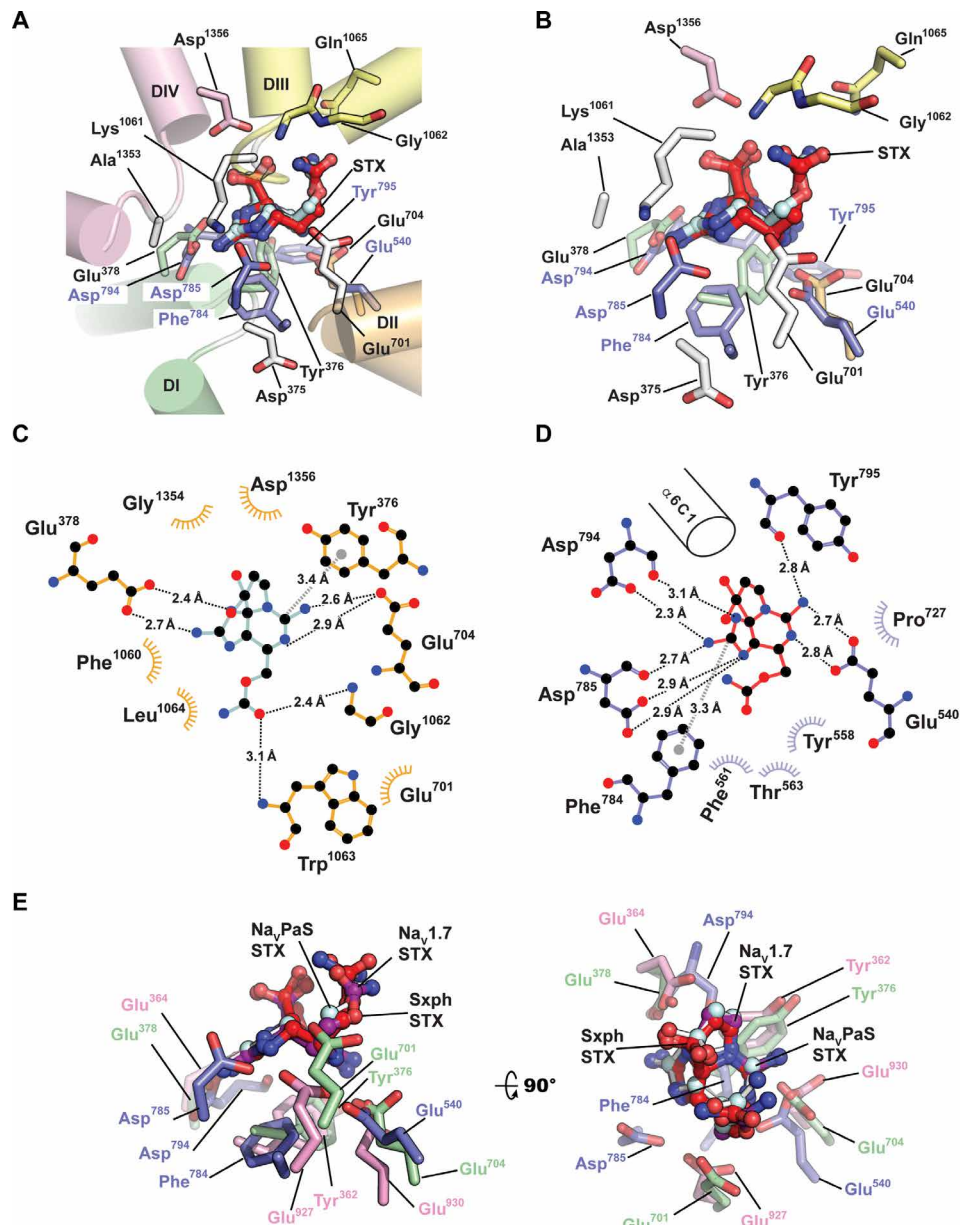


**Fig. 5. Sxph and Na<sub>v</sub>s share STX recognition strategies.** (A) Na<sub>v</sub>PaS:STX (PDB: 6a91) (29) and Sxph:STX STX-binding site superposition. Na<sub>v</sub>PaS is shown as a cartoon viewed from the central channel cavity. Pore domains are colored as follows: DI, green; DII, orange; DIII, yellow; and DIV, pink. STX coordinating and selectivity filter “DEKA” motif (white) residues are shown as sticks. Sxph STX-binding site side chains are blue. STX from Sxph:STX (red) and Na<sub>v</sub>PaS:STX (cyan) are superposed. (B) Closeup view of the STX-binding sites from (A). (C) Diagram of the Na<sub>v</sub>PaS:STX interactions. (D) Diagram of the Sxph:STX interactions. (E) Comparison of common STX interactions for Sxph (blue), Na<sub>v</sub>PaS (green), and Na<sub>v</sub>1.7 (magenta). STX from the Sxph:STX complex (red), Na<sub>v</sub>PaS:STX complex (cyan), and Na<sub>v</sub>1.7:STX complex (violet) are indicated. (C) and (D) were generated using LIGPLOT (67) and a 3.35-Å cutoff. Hydrogen bonding networks (black dashed lines) and cation- $\pi$  interactions (gray dashed lines) are indicated. (D) is the same as Fig. 3C.

How proteins acquire new ligand-binding sites is an unresolved question for which surface pockets are thought to be a key factor (51, 52). Transferrins do not bind STX (35). Structural comparisons of Sxph and transferrins identify a transferrin proto-pocket at cognate position of the Sxph STX-binding site. This region is not known to bind small molecules in any transferrin family member. Nevertheless, the structural data suggest that a limited set of changes are required to reshape this naive site into a high-affinity small-molecule binding site and provide an example of how a protein scaffold can acquire a new function.

Organisms are thought to cope with toxin exposure through diverse strategies that include target protein resistance mutations, toxin sequestration, and toxin removal (10, 11). Frogs are resistant to STX (14, 15), and Sxph may contribute to this property (16, 19). Although how toxin target mutations confer toxin resistance has been widely studied (12, 13, 53), understanding of alternative resistance mechanisms remains primitive. Our findings provide the first structural characterization of a toxin “molecular sponge,” identify an Sxph candidate in a distantly related frog family (*Rainidae* versus *Dicroglossidae*), and provide a starting point for molecular dissection

of toxin sequestration mechanisms. The observation that other organisms have soluble STX-binding proteins unrelated to Sxph (24–28) indicates that toxin sequestration is a general strategy (10, 16, 19) and that de novo STX-binding site creation has happened multiple times.

Defining how proteins recognize STX has implications for understanding its lethal effects, the mechanisms by which organisms evade intoxication, and the design of sensors that could monitor PSP toxins in the environment and food. The Sxph:STX complex structure defined here offers a new path to design protein-based assays for STX and related toxins (7–9, 54), provides a blueprint for STX target identification, and should aid development of STX intoxication countermeasures.

## MATERIALS AND METHODS

### Protein expression and purification

The gene for North American bullfrog, *R. catesbeiana*, Sxph (GenBank: U05246.1), including its N-terminal secretory sequence, was codon-optimized and synthesized by GenScript. The Sxph gene was cloned into the BamHI and HindIII multiple cloning sites of pFastBac1 (Invitrogen) in frame with a C-terminal 3C protease cleavage site, followed by green fluorescent protein (GFP) and a His<sub>10</sub> tag. Bacmids and baculovirus were generated following the manufacturer's protocol (Bac-to-Bac, Invitrogen). P2 baculovirus was used for transduction at dilution of 1:40 into Sf9 cells at cell density of  $2 \times 10^6$  cells ml<sup>-1</sup> in ESF921 media (Expression Systems). Cells were grown for 72 hours after transduction, and the expressed Sxph-GFP fusion protein was secreted into the growth media. Cells were removed by centrifugation, and the supernatant was adjusted to pH 8.0 with a final concentration of 50 mM Tris-HCl and treated with 1 mM NiCl<sub>2</sub> and 5 mM CaCl<sub>2</sub> to precipitate contaminants. Precipitants were removed by centrifugation, and the clarified supernatant was incubated with anti-GFP nanobody-conjugated sepharose beads (55, 56) for 5 hours at room temperature. Beads were washed with 20 column volumes of a buffer containing 300 mM NaCl and 30 mM Tris-HCl (pH 7.4). On-column cleavage of the GFP-His tag was achieved by incubating with 3C protease (0.1 mg ml<sup>-1</sup>) (57) overnight at 4°C. Cleaved sample was further purified by size exclusion chromatography using a Superdex 200 10/300 GL column in buffer containing 150 mM NaCl and 10 mM HEPES (pH 7.4).

### Crystallization and structure determination

Purified Sxph was exchanged into a buffer of 10 mM NaCl and 10 mM HEPES (pH 7.4) and then concentrated to 65 mg ml<sup>-1</sup> using a 50-kDa molecular weight cutoff Amicon Ultra centrifugal filter (Millipore) for crystallization screening by hanging drop vapor diffusion at 4°C using a 2:1 ratio of protein to screening solution. Apo-Sxph was crystallized from solution containing 0.1 M sodium cacodylate (pH 6.5), 5% PEG 8000, and 40% 2-methyl-2,4-pentanediol. Addition of 0.5% β-dodecyl maltoside or 10 mM sodium bromide to the crystallization solution further improved crystal quality of apo-Sxph. Crystals of the Sxph:STX complex were obtained by soaking STX (final concentration, 1 mM) into apo crystals for 5 hours before freezing. For cocrystallization, STX was added to Sxph in a molar ratio of 1.1:1 STX:Sxph. The sample was then incubated on ice for 1 hour before setting up crystallization. X-ray datasets for apo-Sxph and the Sxph:STX complex were collected at Advanced Light Source beamline 8.3.1 (Berkeley, CA) processed with XDS (58) and scaled and merged with Aimless (59). The apo-Sxph structure was deter-

mined by molecular replacement using Phaser from PHENIX (60) and the N-lobe of human serum transferrin (PDB: 1D4N) (61) as a search model. The resulting electron density map was further improved by rigid body refinement using phenix.refine and density modification using RESOLVE (62). The placed starting model was then subjected to model morphing in PHENIX using the prime-and-switch map generated from density modification (63). The morphed model thus allowed subsequent manual model building into the prime-and-switch map in COOT (64). Iterative model building, refinement, density modification, and model morphing allowed the apo-Sxph N-lobe and C1 domain to be built and refined (R-free of 31.7%) but left poor-quality electron density for the entire C2 domain. The feature-enhanced map (FEM) option (65) was applied in PHENIX to aid model building of the Sxph C2 domain. The C2 domain of rabbit serum transferrin (PDB: 1JNF) (41) was used as a starting model and placed into the FEM by rigid-body fitting. Subsequent model rebuilding and refinement were performed in COOT (64) and phenix.refine (60). The structure of the Sxph:STX complex was determined by molecular replacement using apo-Sxph as the search model in Phaser (60). Model building and refinement were carried out using COOT (64) and phenix.refine (60).

### STX synthesis

STX was synthesized, purified, and validated as described in (66).

## SUPPLEMENTARY MATERIALS

Supplementary material for this article is available at <http://advances.sciencemag.org/cgi/content/full/5/6/eaax2650/DC1>

Table S1. Crystallographic data collection and refinement statistics.

Fig. S1. Sxph structural analysis.

Fig. S2. Sxph sequence, secondary structure, and disulfide map.

Fig. S3. Comparison of Sxph and representative transferrin family member sequences.

Fig. S4. Sxph thyroglobulin domain structural analysis.

Fig. S5. STX-binding site and STX derivatives.

Fig. S6. Structural comparison of Sxph N1 and C1 domains.

Fig. S7. Sequence comparison of Sxph and putative Sxph homologs.

Fig. S8. Na<sub>v</sub>PaS:STX and Na<sub>v</sub>1.7:STX interactions.

Movie S1. Sxph conformational changes upon STX binding.

References (68–71)

## REFERENCES AND NOTES

1. A. P. Thottumkara, W. H. Parsons, J. Du Bois, Saxitoxin. *Angew. Chem. Int. Ed. Engl.* **53**, 5760–5784 (2014).
2. L. M. Duran-Riveroll, A. D. Cembella, Guanidinium toxins and their interactions with voltage-gated sodium ion channels. *Mar. Drugs* **15**, 303 (2017).
3. B. Hille, *Ion Channels of Excitable Membranes* (Sinauer Associates Inc., ed. 3, 2001).
4. Z. Su, M. Sheets, H. Ishida, F. Li, W. H. Barry, Saxitoxin blocks L-type I<sub>Ca</sub>. *J. Pharmacol. Exp. Ther.* **308**, 324–329 (2004).
5. J. Wang, J. J. Salata, P. B. Bennett, Saxitoxin is a gating modifier of HERG K<sup>+</sup> channels. *J. Gen. Physiol.* **121**, 583–598 (2003).
6. L. E. Llewellyn, Saxitoxin, a toxic marine natural product that targets a multitude of receptors. *Nat. Prod. Rep.* **23**, 200–222 (2006).
7. K. Campbell, D. F. Rawn, B. Niedzwiedek, C. T. Elliott, Paralytic shellfish poisoning (PSP) toxin binders for optical biosensor technology: Problems and possibilities for the future: A review. *Food Addit. Contam. Part A Chem. Anal. Control Expo. Risk Assess.* **28**, 711–725 (2011).
8. AOAC, in *Official Methods of Analysis* (Arlington, VA, 1999), vol. 1.
9. S. R. Ruberu, G. W. Langlois, M. Masuda, C. Kittredge, S. K. Perera, R. M. Kudela, Receptor binding assay for the detection of paralytic shellfish poisoning toxins: Comparison to the mouse bioassay and applicability under regulatory use. *Food Addit. Contam. Part A Chem. Anal. Control Expo. Risk Assess.* **35**, 144–158 (2017).
10. K. H. Almagbruk, L. K. Dinh, B. Philmus, Self-resistance of natural product producers: Past, present, and future focusing on self-resistant protein variants. *ACS Chem. Biol.* **13**, 1426–1437 (2018).

11. P. Hunter, Do not poison thyself: Mechanisms to avoid self-toxicity could inspire novel compounds and pathways for synthetic biology and applications for agriculture. *EMBO Rep.* **19**, e46756 (2018).
12. R. D. Tarvin, C. M. Borghese, W. Sachs, J. C. Santos, Y. Lu, L. A. O'Connell, D. C. Cannatella, R. A. Harris, H. H. Zakon, Interacting amino acid replacements allow poison frogs to evolve epibatidine resistance. *Science* **357**, 1261–1266 (2017).
13. V. M. Briceelj, L. Connell, K. Konoki, S. P. MacQuarrie, T. Scheuer, W. A. Catterall, V. L. Trainer, Sodium channel mutation leading to saxitoxin resistance in clams increases risk of PSP. *Nature* **434**, 763–767 (2005).
14. M. Prinzmetal, H. Sommer, C. D. Leake, The pharmacological action of "mussel poison". *J. Pharmacol. Exp. Ther.* **46**, 63–73 (1932).
15. C. Y. Kao, F. A. Fuhrman, Differentiation of the actions of tetrodotoxin and saxitoxin. *Toxicon* **5**, 25–34 (1967).
16. J. Mahar, G. L. Lukács, Y. Li, S. Hall, E. Moczydlowski, Pharmacological and biochemical properties of saxiphilin, a soluble saxitoxin-binding protein from the bullfrog (*Rana catesbeiana*). *Toxicon* **29**, 53–71 (1991).
17. D. D. Doyle, M. Wong, J. Tanaka, L. Barr, Saxitoxin binding sites in frog-myocardial cytosol. *Science* **215**, 1117–1119 (1982).
18. M. A. Morabito, E. Moczydlowski, Molecular cloning of bullfrog saxiphilin: A unique relative of the transferrin family that binds saxitoxin. *Proc. Natl. Acad. Sci. U.S.A.* **91**, 2478–2482 (1994).
19. L. E. Llewellyn, P. M. Bell, E. G. Moczydlowski, Phylogenetic survey of soluble saxitoxin-binding activity in pursuit of the function and molecular evolution of saxiphilin, a relative of transferrin. *Proc. R. Soc. B* **264**, 891–902 (1997).
20. L. E. Llewellyn, E. G. Moczydlowski, Characterization of saxitoxin binding to saxiphilin, a relative of the transferrin family that displays pH-dependent ligand binding. *Biochemistry* **33**, 12312–12322 (2002).
21. M. A. Morabito, L. E. Llewellyn, E. G. Moczydlowski, Expression of saxiphilin in insect cells and localization of the saxitoxin-binding site to the C-terminal domain homologous to the C-lobe of transferrins. *Biochemistry* **34**, 13027–13033 (1995).
22. P. Lewis, I. Fritsch, R. E. Gawley, R. Henry, A. Kight, J. O. Lay Jr., R. Liyanage, J. McLachlin, Dynamics of saxitoxin binding to saxiphilin c-lobe reveals conformational change. *Toxicon* **51**, 208–217 (2008).
23. B. Lenarčič, G. Krishnan, R. Borukhovich, B. Ruck, V. Turk, E. Moczydlowski, Saxiphilin, a saxitoxin-binding protein with two thyroglobulin type 1 domains, is an inhibitor of papain-like cysteine proteinases. *J. Biol. Chem.* **275**, 15572–15577 (2000).
24. M. Yotsu-Yamashita, A. Sugimoto, T. Terakawa, Y. Shoji, T. Miyazawa, T. Yasumoto, Purification, characterization, and cDNA cloning of a novel soluble saxitoxin and tetrodotoxin binding protein from plasma of the puffer fish, *Fugu pardalis*. *Eur. J. Biochem.* **268**, 5937–5946 (2001).
25. M. Yotsu-Yamashita, H. Yamaki, N. Okoshi, N. Araki, Distribution of homologous proteins to puffer fish saxitoxin and tetrodotoxin binding protein in the plasma of puffer fish and among the tissues of *Fugu pardalis* examined by Western blot analysis. *Toxicon* **55**, 1119–1124 (2010).
26. N. Takati, D. Mountassif, H. Taleb, K. Lee, M. Blaghen, Purification and partial characterization of paralytic shellfish poison-binding protein from *Acanthocardia tuberculatum*. *Toxicon* **50**, 311–321 (2007).
27. H. Lin, C. Zhang, J. Liao, F. Yang, S. Zhong, P. Jiang, X. Chen, Y. Nagashima, Neutralizing effect of hemolymph from the shore crab, *Thalassia crenata*, on paralytic shellfish toxins. *Toxicon* **99**, 51–57 (2015).
28. J. C. Tanaka, D. D. Doyle, L. Barr, Sodium channels in vertebrate hearts. Three types of saxitoxin binding sites in heart. *Biochim. Biophys. Acta* **775**, 203–214 (1984).
29. H. Shen, Z. Li, Y. Jiang, X. Pan, J. Wu, B. Cristofori-Armstrong, J. J. Smith, Y. K. Y. Chin, J. Lei, Q. Zhou, G. F. King, N. Yan, Structural basis for the modulation of voltage-gated sodium channels by animal toxins. *Science* **362**, eaau2596 (2018).
30. L. A. Lambert, Molecular evolution of the transferrin family and associated receptors. *Biochim. Biophys. Acta* **1820**, 244–255 (2012).
31. K. Mizutani, M. Toyoda, B. Mikami, X-ray structures of transferrins and related proteins. *Biochim. Biophys. Acta* **1820**, 203–211 (2012).
32. J. Wally, P. J. Halbrooks, C. Vornheim, M. A. Rould, S. J. Everse, A. B. Mason, S. K. Buchanan, The crystal structure of iron-free human serum transferrin provides insight into inter-lobe communication and receptor binding. *J. Biol. Chem.* **281**, 24934–24944 (2006).
33. L. A. Lambert, H. Perri, P. J. Halbrooks, A. B. Mason, Evolution of the transferrin family: Conservation of residues associated with iron and anion binding. *Comp. Biochem. Physiol. B Biochem. Mol. Biol.* **142**, 129–141 (2005).
34. R. T. A. MacGillivray, S. A. Moore, J. Chen, B. F. Anderson, H. Baker, Y. Luo, M. Bewley, C. A. Smith, M. E. P. Murphy, Y. Wang, A. B. Mason, R. C. Woodworth, G. D. Brayer, E. N. Baker, Two high-resolution crystal structures of the recombinant N-lobe of human transferrin reveal a structural change implicated in iron release. *Biochemistry* **37**, 7919–7928 (1998).
35. Y. Li, L. Llewellyn, E. Moczydlowski, Biochemical and immunochemical comparison of saxiphilin and transferrin, two structurally related plasma proteins from *Rana catesbeiana*. *Mol. Pharmacol.* **44**, 742–748 (1993).
36. Y. Malthiéry, S. Lissitzky, Primary structure of human thyroglobulin deduced from the sequence of its 8448-base complementary DNA. *Eur. J. Biochem.* **165**, 491–498 (1987).
37. B. Lenarčič, T. Bevec, Thyropins—New structurally related proteinase inhibitors. *Biol. Chem.* **379**, 105–111 (1998).
38. G. Gunčar, G. Pungerič, I. Klemenčič, V. Turk, D. Turk, Crystal structure of MHC class II-associated p41 li fragment bound to cathepsin L reveals the structural basis for differentiation between cathepsins L and S. *EMBO J.* **18**, 793–803 (1999).
39. F. Molina, M. Bouanani, B. Pau, C. Granier, Characterization of the type-1 repeat from thyroglobulin, a cysteine-rich module found in proteins from different families. *Eur. J. Biochem.* **240**, 125–133 (1996).
40. M. Novinec, D. Kordiš, V. Turk, B. Lenarčič, Diversity and evolution of the thyroglobulin type-1 domain superfamily. *Mol. Biol. Evol.* **23**, 744–755 (2006).
41. D. R. Hall, J. M. Hadden, G. A. Leonard, S. Bailey, M. Neu, M. Winn, P. F. Lindley, The crystal and molecular structures of ferret porcine and rabbit serum transferrins at resolutions of 2.15 and 2.60 Å, respectively. *Acta Crystallogr. D Biol. Crystallogr.* **58**, 70–80 (2002).
42. W. H. Parsons, J. Du Bois, Maleimide conjugates of saxitoxin as covalent inhibitors of voltage-gated sodium channels. *J. Am. Chem. Soc.* **135**, 10582–10585 (2013).
43. C. Y. Kao, P. N. Kao, M. R. James-Kracc, F. E. Koehn, C. F. Wichmann, H. K. Schnoes, Actions of equimers of 12-(OH)-reduced saxitoxin and of 11-(Oso<sub>3</sub>)-saxitoxin on squid axon. *Toxicon* **23**, 647–655 (1985).
44. J. L. Penzotti, H. A. Fozzard, G. M. Lipkind, S. C. Dudley Jr., Differences in saxitoxin and tetrodotoxin binding revealed by mutagenesis of the Na<sup>+</sup> channel outer vestibule. *Biophys. J.* **75**, 2647–2657 (1998).
45. R. Thomas-Tran, J. Du Bois, Mutant cycle analysis with modified saxitoxins reveals specific interactions critical to attaining high-affinity inhibition of hNa<sub>v</sub>1.7. *Proc. Natl. Acad. Sci. U.S.A.* **113**, 5856–5861 (2016).
46. J. Satin, J. W. Kyle, M. Chen, P. Bell, L. L. Cribbs, H. A. Fozzard, R. B. Rogart, A mutant of TTX-resistant cardiac sodium channels with TTX-sensitive properties. *Science* **256**, 1202–1205 (1992).
47. H. Shen, D. Liu, K. Wu, J. Lei, N. Yan, Structures of human Na<sub>v</sub>1.7 channel in complex with auxiliary subunits and animal toxins. *Science* **363**, 1303–1308 (2019).
48. B. A. Barad, N. Echols, R. Y.-R. Wang, Y. Cheng, F. DiMaio, P. D. Adams, J. S. Fraser, EMRinger: Side chain-directed model and map validation for 3D cryo-electron microscopy. *Nat. Methods* **12**, 943–946 (2015).
49. A. Bartesaghi, D. Matthies, S. Banerjee, A. Merk, S. Subramaniam, Structure of β-galactosidase at 3.2-Å resolution obtained by cryo-electron microscopy. *Proc. Natl. Acad. Sci. U.S.A.* **111**, 11709–11714 (2014).
50. J. Vonck, D. J. Mills, Advances in high-resolution cryo-EM of oligomeric enzymes. *Curr. Opin. Struct. Biol.* **46**, 48–54 (2017).
51. R. A. Laskowski, N. M. Luscombe, M. B. Swindells, J. M. Thornton, Protein clefts in molecular recognition and function. *Protein Sci.* **5**, 2438–2452 (1996).
52. M. Gao, J. Skolnick, The distribution of ligand-binding pockets around protein-protein interfaces suggests a general mechanism for pocket formation. *Proc. Natl. Acad. Sci. U.S.A.* **109**, 3784–3789 (2012).
53. S. L. Gefken, E. Fujimoto, E. D. Brodie III, E. D. Brodie Jr., P. C. Ruben, Evolutionary diversification of TTX-resistant sodium channels in a predator-prey interaction. *Nature* **434**, 759–763 (2005).
54. L. E. Llewellyn, J. Doyle, J. Jellett, R. Barrett, C. Alison, C. Bentz, M. Quilliam, Measurement of paralytic shellfish toxins in molluscan extracts: Comparison of the microtitre plate saxiphilin and sodium channel radioreceptor assays with mouse bioassay, HPLC analysis and a commercially available cell culture assay. *Food Addit. Contam.* **18**, 970–980 (2001).
55. M. Lolicato, C. Arrigoni, T. Mori, Y. Sekioka, C. Bryant, K. A. Clark, D. L. Minor Jr., K<sub>2p</sub>2.1 (TREK-1)-activator complexes reveal a cryptic selectivity filter binding site. *Nature* **547**, 364–368 (2017).
56. P. C. Fridy, Y. Li, S. Keegan, M. K. Thompson, I. Nudelman, J. F. Scheid, M. Oeffinger, M. C. Nussenzweig, D. Fenyö, B. T. Chait, M. P. Rout, A robust pipeline for rapid production of versatile nanobody repertoires. *Nat. Methods* **11**, 1253–1260 (2014).
57. D. Shaya, M. Kreir, R. A. Robbins, S. Wong, J. Hammon, A. Bruggemann, D. L. Minor Jr., Voltage-gated sodium channel (Na<sub>v</sub>) protein dissection creates a set of functional pore-only proteins. *Proc. Natl. Acad. Sci. U.S.A.* **108**, 12313–12318 (2011).
58. W. Kabsch, XDS. *Acta Crystallogr. D Biol. Crystallogr.* **66**, 125–132 (2010).
59. P. R. Evans, G. N. Murshudov, How good are my data and what is the resolution? *Acta Crystallogr. D Biol. Crystallogr.* **69**, 1204–1214 (2013).
60. P. D. Adams, P. V. Afonine, G. Bunkóczi, V. B. Chen, I. W. Davis, N. Echols, J. J. Headd, L.-W. Hung, G. J. Kapral, R. W. Grosse-Kunstleve, A. J. McCoy, N. W. Moriarty, R. Oeffner, R. J. Read, D. C. Richardson, J. S. Richardson, T. C. Terwilliger, P. H. Zwart, PHENIX: A comprehensive Python-based system for macromolecular structure solution. *Acta Crystallogr. D Biol. Crystallogr.* **66**, 213–221 (2010).

61. A. H. W. Yang, R. T. A. MacGillivray, J. Chen, Y. Luo, Y. Wang, G. D. Brayer, A. B. Mason, R. C. Woodworth, M. E. Murphy, Crystal structures of two mutants (K206Q, H207E) of the N-lobe of human transferrin with increased affinity for iron. *Protein Sci.* **9**, 49–52 (2000).
62. T. Terwilliger, SOLVE and RESOLVE: Automated structure solution, density modification and model building. *J. Synchrotron Radiat.* **11**, 49–52 (2004).
63. T. C. Terwilliger, R. J. Read, P. D. Adams, A. T. Brunger, P. V. Afonine, L. W. Hung, Model morphing and sequence assignment after molecular replacement. *Acta Crystallogr. D Biol. Crystallogr.* **69**, 2244–2250 (2013).
64. P. Emsley, K. Cowtan, Coot: Model-building tools for molecular graphics. *Acta Crystallogr. D Biol. Crystallogr.* **60**, 2126–2132 (2004).
65. P. V. Afonine, N. W. Moriarty, M. Mustyakimov, O. V. Sobolev, T. C. Terwilliger, D. Turk, A. Urzhumtsev, P. D. Adams, FEM: Feature-enhanced map. *Acta Crystallogr. D Biol. Crystallogr.* **71**, 646–666 (2015).
66. J. R. Walker, J. E. Merit, R. Thomas-Tran, D. T. Y. Tang, J. Du Bois, Divergent synthesis of natural derivatives of (+)-saxitoxin including 11-saxitoxinethanoic acid. *Angew. Chem. Int. Ed. Engl.* **58**, 1689–1693 (2019).
67. A. C. Wallace, R. A. Laskowski, J. M. Thornton, LIGPLOT: A program to generate schematic diagrams of protein-ligand interactions. *Protein Eng.* **8**, 127–134 (1995).
68. E. Schröder, C. Phillips, E. Garman, K. Harlos, C. Crawford, X-ray crystallographic structure of a papain-leupeptin complex. *FEBS Lett.* **315**, 38–42 (1993).
69. A. Sala, S. Capaldi, M. Campagnoli, B. Faggion, S. Labò, M. Perduca, A. Romano, M. E. Carrizo, M. Valli, L. Visai, L. Minchiotti, M. Galliano, H. L. Monaco, Structure and properties of the C-terminal domain of insulin-like growth factor-binding protein-1 isolated from human amniotic fluid. *J. Biol. Chem.* **280**, 29812–29819 (2005).
70. T. Sitar, G. M. Popowicz, I. Siwanowicz, R. Huber, T. A. Holak, Structural basis for the inhibition of insulin-like growth factors by insulin-like growth factor-binding proteins. *Proc. Natl. Acad. Sci. U.S.A.* **103**, 13028–13033 (2006).
71. M. Pavšič, G. Gunčar, K. Djinović-Carugo, B. Lenarčič, Crystal structure and its bearing towards an understanding of key biological functions of EpCAM. *Nat. Commun.* **5**, 4764 (2014).

**Acknowledgments:** We thank C. Kimberlin and Y. Wu for help with molecular biology and protein expression, and F. Abderemane-Ali, K. Brejc, and J. Dumbacher for comments on the manuscript. **Funding:** This work was supported by grants NIH-NHLBI R01-HL080050 to D.L.M., NIH-NIGMS GM117263-01A1 to J.D.B., and an NSF Graduate Research Fellowship to R.T.-T. **Author contributions:** T.-J.Y. and D.L.M. conceived the study and designed the experiments. T.-J.Y. performed molecular biology experiments, expressed, purified, and crystallized the proteins, and collected diffraction data. T.-J.Y. and M.L. determined the structures. R.T.-T. synthesized STX. J.D.B. and D.L.M. analyzed data and provided guidance and support. T.-J.Y., M.L., J.D.B., and D.L.M. wrote the paper. **Competing interests:** J.D.B. is a cofounder and holds equity shares in SiteOne Therapeutics Inc., a start-up company interested in developing subtype-selective modulators of sodium channels. The other authors declare that they no competing interests. **Data and materials availability:** All data needed to evaluate the conclusions in the paper are present in the paper and/or the Supplementary Materials. Coordinates and structure factors are deposited in the RCSB under accession codes 6O0D, 6O0E, and 6O0F for apo-Sxph, Sxph:STX (soaked), and Sxph:STX (cocrystallized), respectively, and will be released immediately upon publication. Additional data related to this paper may be requested from the authors.

Submitted 7 March 2019  
Accepted 13 May 2019  
Published 19 June 2019  
10.1126/sciadv.aax2650

**Citation:** T.-J. Yen, M. Lolicato, R. Thomas-Tran, J. Du Bois, D. L. Minor Jr., Structure of the saxiphilin:saxitoxin (STX) complex reveals a convergent molecular recognition strategy for paralytic toxins. *Sci. Adv.* **5**, eaax2650 (2019).

## Structure of the saxiphilin:saxitoxin (STX) complex reveals a convergent molecular recognition strategy for paralytic toxins

Tien-Jui Yen, Marco Lolicato, Rhiannon Thomas-Tran, J. Du Bois and Daniel L. Minor, Jr.

*Sci Adv* 5 (6), eaax2650.  
DOI: 10.1126/sciadv.aax2650

ARTICLE TOOLS	<a href="http://advances.sciencemag.org/content/5/6/eaax2650">http://advances.sciencemag.org/content/5/6/eaax2650</a>
SUPPLEMENTARY MATERIALS	<a href="http://advances.sciencemag.org/content/suppl/2019/06/17/5.6.eaax2650.DC1">http://advances.sciencemag.org/content/suppl/2019/06/17/5.6.eaax2650.DC1</a>
REFERENCES	This article cites 68 articles, 20 of which you can access for free <a href="http://advances.sciencemag.org/content/5/6/eaax2650#BIBL">http://advances.sciencemag.org/content/5/6/eaax2650#BIBL</a>
PERMISSIONS	<a href="http://www.sciencemag.org/help/reprints-and-permissions">http://www.sciencemag.org/help/reprints-and-permissions</a>

Use of this article is subject to the [Terms of Service](#)

## Supplementary Materials for

### **Structure of the saxiphilin:saxitoxin (STX) complex reveals a convergent molecular recognition strategy for paralytic toxins**

Tien-Jui Yen, Marco Lolicato, Rhiannon Thomas-Tran, J. Du Bois, Daniel L. Minor Jr.\*

\*Corresponding author. Email: [daniel.minor@ucsf.edu](mailto:daniel.minor@ucsf.edu)

Published 19 June 2019, *Sci. Adv.* **5**, eaax2650 (2019)

DOI: 10.1126/sciadv.aax2650

#### **The PDF file includes:**

Table S1. Crystallographic data collection and refinement statistics.  
Fig. S1. Sxph structural analysis.  
Fig. S2. Sxph sequence, secondary structure, and disulfide map.  
Fig. S3. Comparison of Sxph and representative transferrin family member sequences.  
Fig. S4. Sxph thyroglobulin domain structural analysis.  
Fig. S5. STX-binding site and STX derivatives.  
Fig. S6. Structural comparison of Sxph N1 and C1 domains.  
Fig. S7. Sequence comparison of Sxph and putative Sxph homologs.  
Fig. S8. Na<sub>v</sub>PaS:STX and Na<sub>v</sub>1.7:STX interactions.  
Legend for movie S1  
References (68–71)

#### **Other Supplementary Material for this manuscript includes the following:**

(available at [advances.sciencemag.org/cgi/content/full/5/6/eaax2650/DC1](https://advances.sciencemag.org/cgi/content/full/5/6/eaax2650/DC1))

Movie S1 (.mp4 format). Sxph conformational changes upon STX binding.

**Table S1. Crystallographic data collection and refinement statistics.**

	<b>apo-Saxiphilin</b>	<b>Sxph:STX complex (soaked)</b>	<b>Sxph:STX complex (co-crystal)</b>
<b>Data Collection</b>			
Space group	P2 <sub>1</sub> 2 <sub>1</sub> 2 <sub>1</sub>	P2 <sub>1</sub> 2 <sub>1</sub> 2 <sub>1</sub>	P2 <sub>1</sub> 2 <sub>1</sub> 2 <sub>1</sub>
Unit cell			
a, b, c (Å) <sup>a</sup>	96.2, 111.3, 254.8	96.4, 110.8, 254.6	96.6, 111.7, 254.6
α, β, γ (°)	90, 90, 90	90, 90, 90	90, 90, 90
Resolution (Å)	48.2-2.50 (2.54-2.50)	48.2-2.50 (2.54-2.50)	48.3- 2.12 (2.16-2.12)
Total reflections	1143210	1155387	1962129
Unique reflections	95268	94650	156355
Completeness (%)	99.8 (97.3)	99.6 (95.2)	99.9 (98.5)
Redundancy	12.0 (6.6)	12.2 (6.7)	12.5 (7.4)
I/σI	16.0 (1.1)	14.7 (0.5)	13.3 (0.3)
CC <sub>1/2</sub>	1 (0.57)	1 (0.25)	1 (0.10)
<b>Refinement<sup>b</sup></b>			
R <sub>work</sub> (%)	22.4	23.7	23.8
R <sub>free</sub> (%)	25.3	26.2	25.9
RMS deviations			
Bonds (Å)	0.003	0.003	0.002
Angles (°)	0.68	0.76	0.68
Average B factor	83.3	105.0	94.2
Protein	83.6	105.1	94.6
Water	59.5	69.7	69.4
Ligand	-	116.1	95.1
Ramachandran [%]			
Allowed/generous/disallowed	95.2/4.0/0.8	93.8/5.0/1.2	95.3/3.6/1.1

<sup>a</sup> statistics for the highest resolution shell are shown in parentheses.

<sup>b</sup> Final refined models cover all residues except for the following:

**apo-Saxiphilin**

Chain A, 171-178, 289, 571-573, 620, and 637-646

Chain B, 1-4 and 169-178

**Sxph:STX complex (soaked)**

Chain A : 1-3, 172-177, 585-586, 620-621, 637-647, 673-674, 701-711, and 717-718

Chain B: 1-4, 169-179, and 572-573

**Sxph:STX complex (co-crystal)**

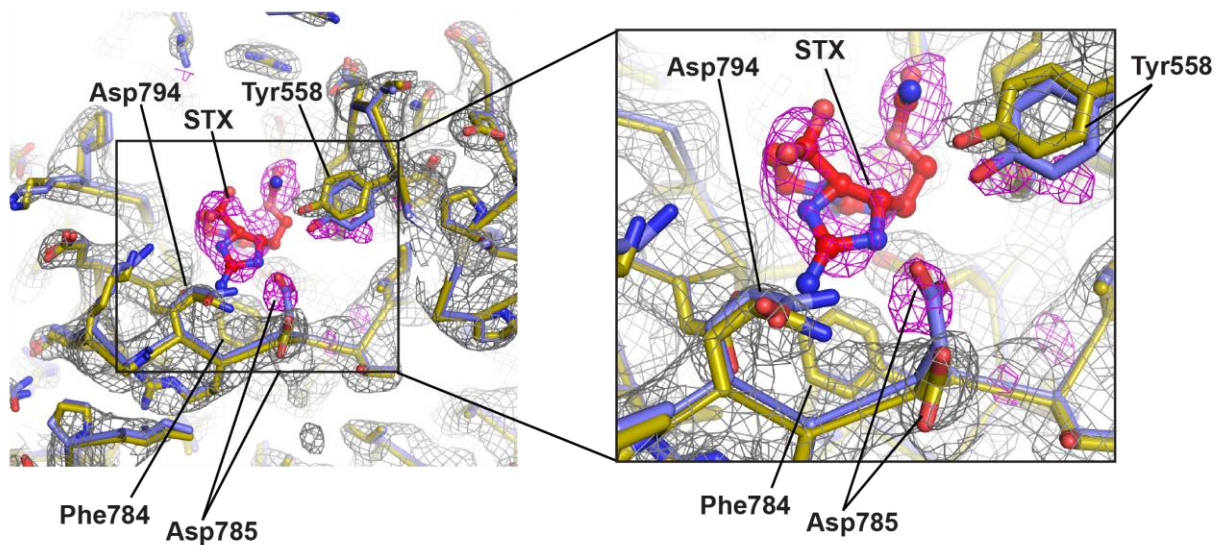
Chain A : 1,2, 171-173, 585-586, 620-621, 637-647, 673-674

Chain B: 1-4, 169-178, and 572-573

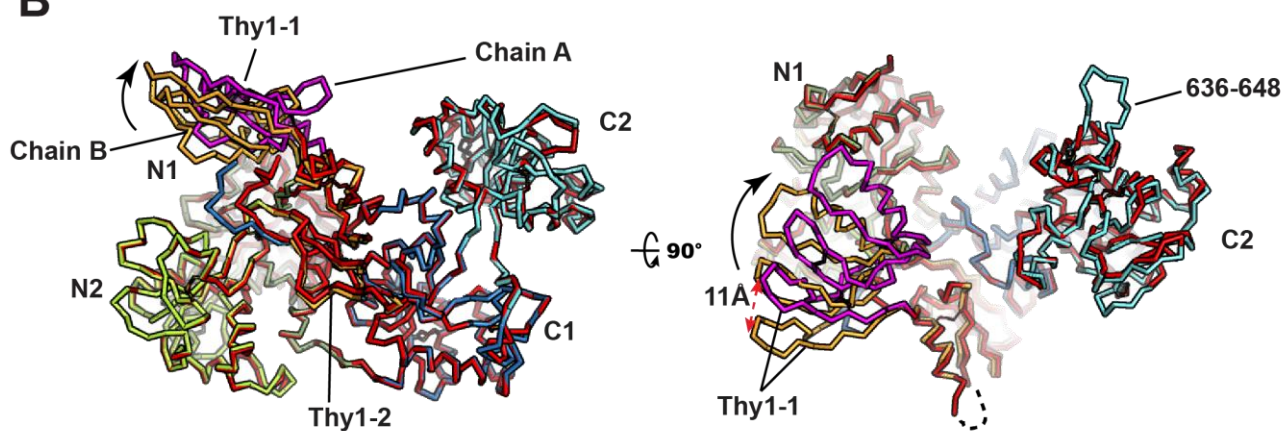
Fig. S1

Yen *et al.*

A



B



C

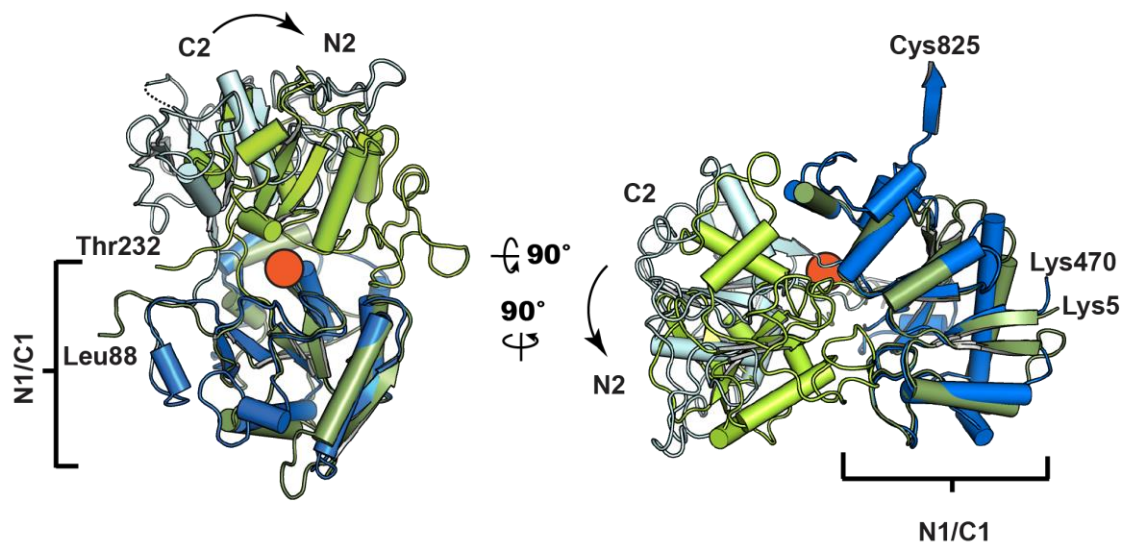


**Fig. S1. Sxph structural analysis.** **(A)** Exemplar 2Fo-Fc electron density ( $1.5\sigma$ )(grey) and Fo-Fo ( $5\sigma$ )(magenta) for Sxph and STX, respectively. Sxph (olive) and Sxph:STX (marine) are shown and select residues are labeled. STX is red. **(B)** Ribbon diagram superposition of apo-Sxph Chain A (red and magenta) and Chain B ( $\text{RMSD}_{\text{C}\alpha} = 0.61 \text{ \AA}$  over 663 residues). Chain A Thy1-1 is colored magenta. Chain B subdomains are colored: N1 (smudge), N2 (Limon), Thy (bright orange), C1 (marine), and C2 (cyan). Relative displacement of the Thy1-1 is indicated. **(C)** Superposition of apo-Sxph N-lobe (N1, smudge; N2, limon) and C-lobe (C1, marine; C2, cyan). Relative motions of N2 and C2 subdomains are indicated. As a point of reference, the orange sphere marks position that corresponds to the transferrin  $\text{Fe}^{3+}$  binding site. The N-lobe and C1 cores have lowest B-factors (average B factor of  $74.0 \text{ \AA}^2$  for N-lobe and  $63.4 \text{ \AA}^2$  for C1 domain), whereas the majority of C2 is more mobile (average B-factor of  $108.4 \text{ \AA}^2$ ).

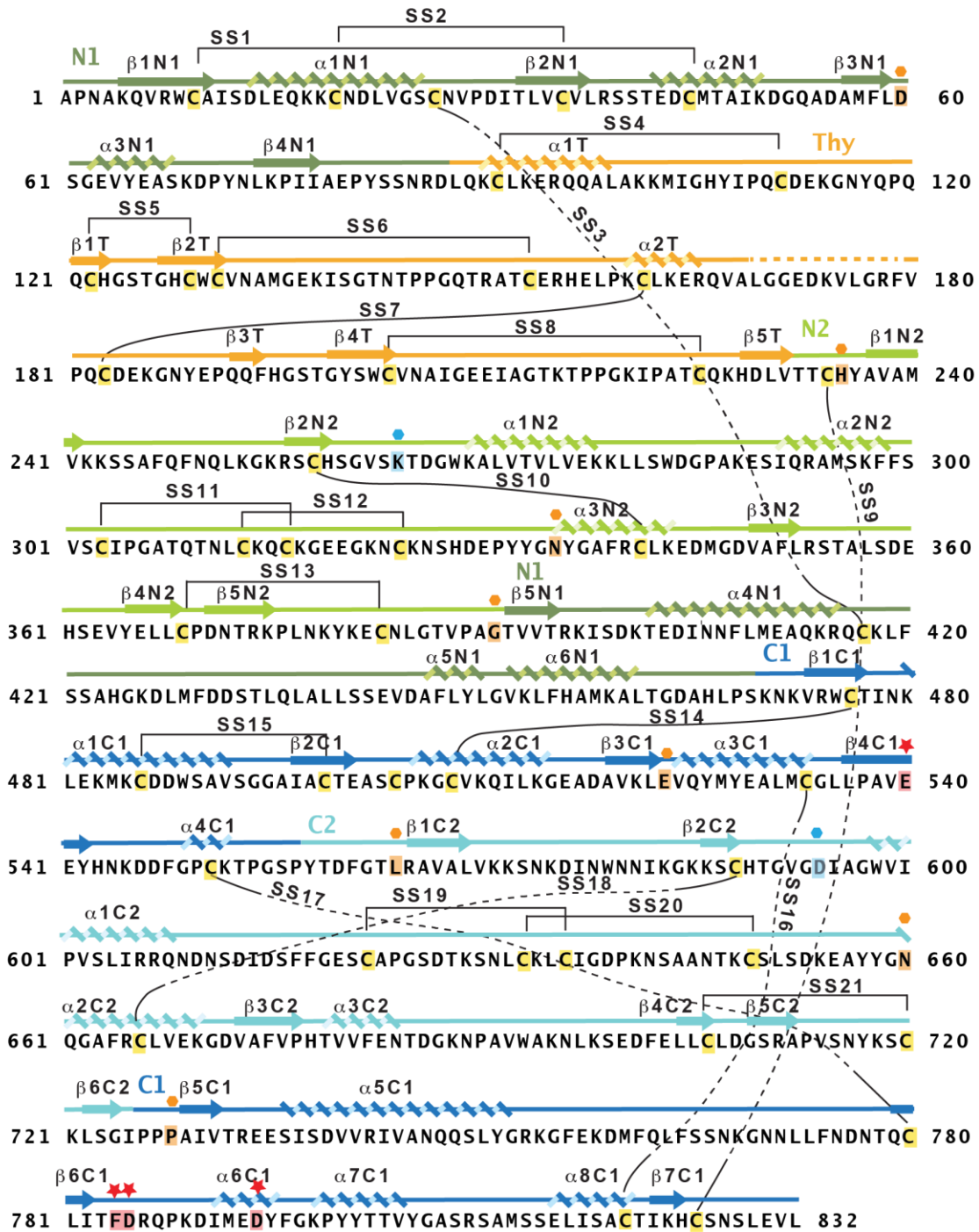


**Fig. S2. Sxph sequence, secondary structure, and disulfide map.** *Rana catesbeiana* Sxph sequence. Secondary structures are indicated. Domains are labeled and colored as in fig. S1A. Cysteine residues (yellow) and disulfide bonds (SS#) are indicated. Residues corresponding to transferrin Fe<sup>3+</sup> and carbonate ligands are indicated by orange and blue hexagons, respectively and highlighted. Residues corresponding to STX-interacting residues are indicated by the red star and are highlighted.

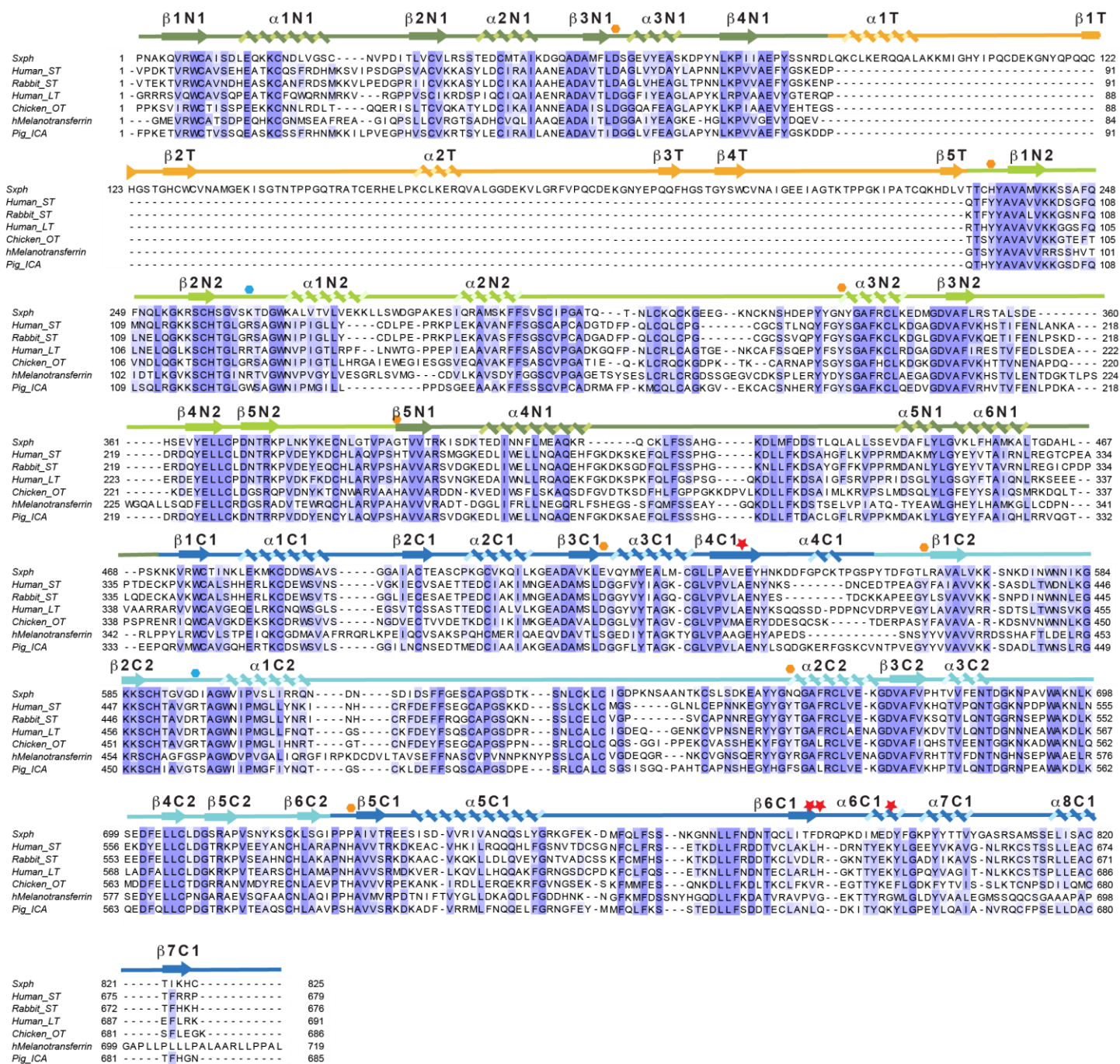
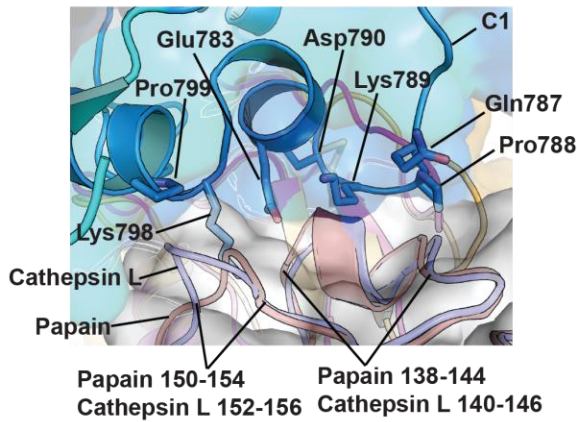


**Fig. S3. Comparison of Sxph and representative transferrin family member sequences.**

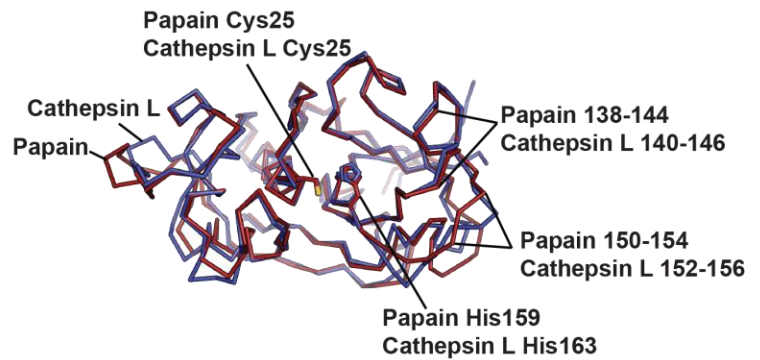
Sequence alignment of *Rana catesbeiana* Sxph with representative members of the transferrin family. Human serum transferrin (Human\_ST) (UniProtKB: P02787), rabbit serum transferrin (Rabbit\_ST) (UniProtKB:P19134), human lactotransferrin (Human\_LT) (UniProtKB:P02788), chicken ovotransferrin (Chicken\_OT) (UniProtKB:P02789), human melanotransferrin (Melanotransferrin) (UniProtKB:P08582), and pig inhibitor of carbonic anhydrase (Pig\_ICA) (UniProtKB:Q29545). Sxph

domain and secondary structures are indicated and colored as in fig. S1B. Residues corresponding to transferrin  $\text{Fe}^{3+}$  and carbonate ligands are indicated by orange and blue hexagons, respectively and highlighted (38).

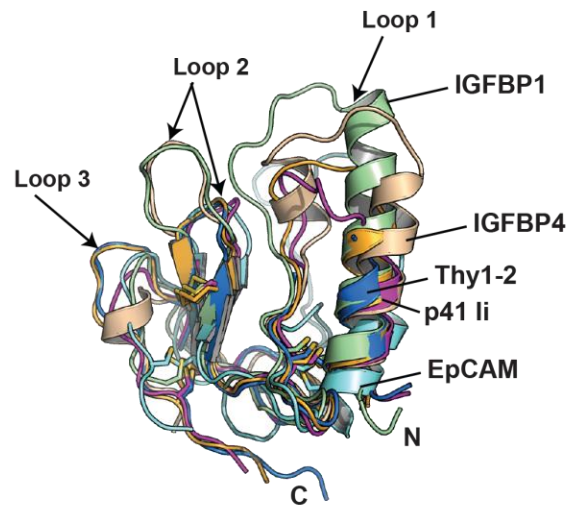
**A**



**B**



**C**



**D**

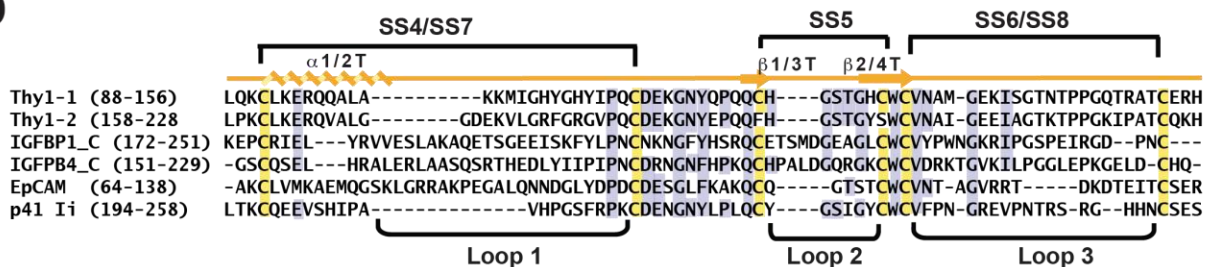


**Fig. S4. Sxph thyroglobulin domain structural analysis.** (A) Close up view of the superposition of the Sxph Thy1-2 domain on the p41 li:cathepsin L complex and papain (PDB: 1POP) (68) on the p41:cathepsin L complex (PDB: 1ICF) (38). Sxph residues that clash with the enzyme surface are labeled. Regions of cathepsin L (light blue) and papain (firebrick) are indicated. (B) Superposition of cathepsin L from the p41 li:cathepsin complex (PDB: 1ICF) (38) and papain (PDB: 1POP) (68).  $RMSD_{C\alpha} = 0.66 \text{ \AA}$  over 168 residues. Active site residues and regions of clash from panel 'A' are indicated and clash with Sxph C1 residues 787-790, 783, and 787-799. (C) Superposition of Thy1

domains from Sxph (Thy1-1, bright orange, Thy1-2, marine), p41 (1ICF, magenta) (38), IGFBP1 (1ZT3, green) (69), IGPBP4 (PDB: 2DSR, wheat)(70), and EpCAM (PDB: 4MZV, aquamarine)(71).  
**(D)** Sequence comparison of Thy1 domains from 'C'. Secondary structure elements and disulfide bond labels are from the Sxph Thy1 domains.

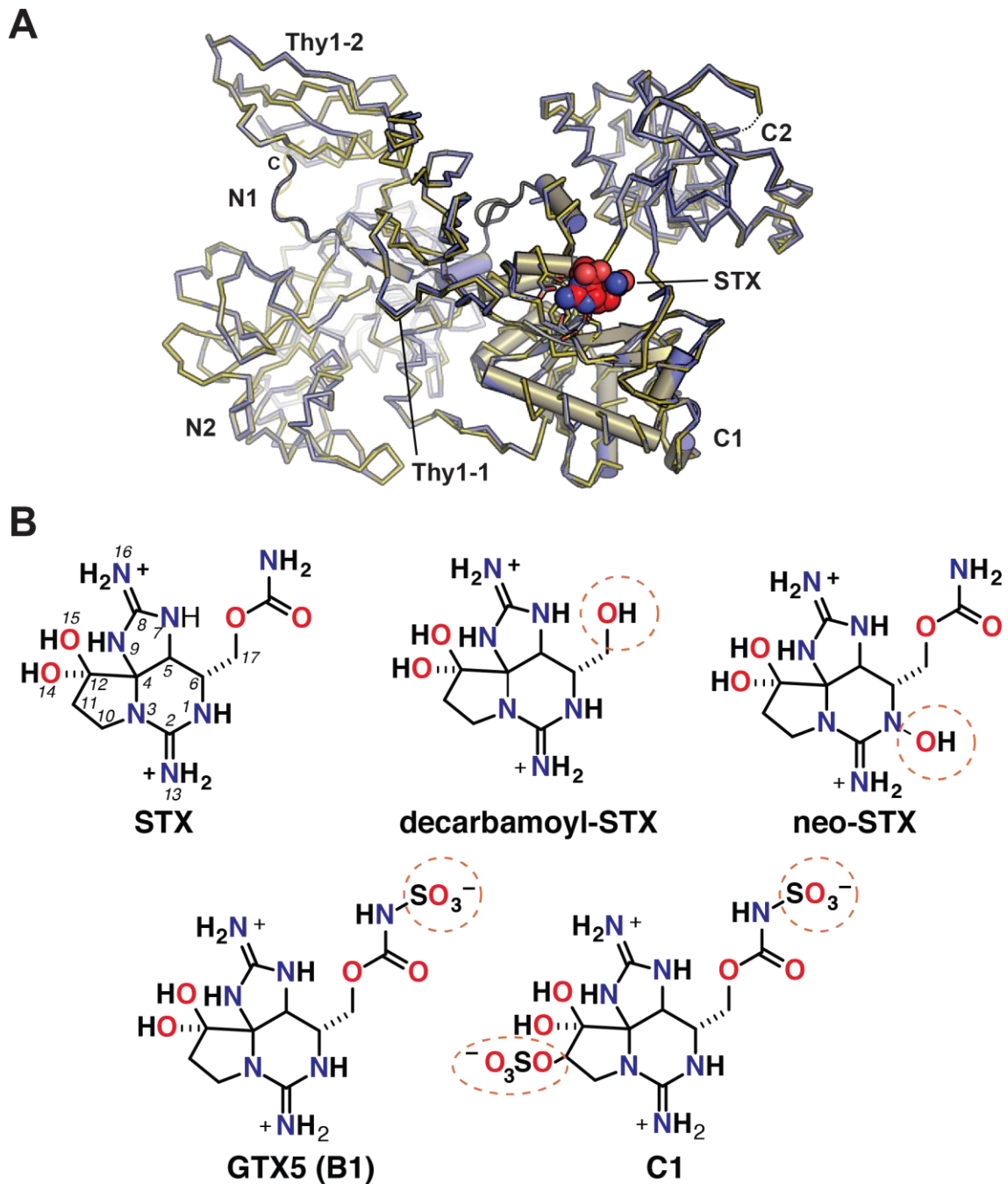


**Fig. S5. STX-binding site and STX derivatives.** (A) Superposition of apo-Sxph (olive) and STX bound STX (slate) shown as ribbons ( $\text{RMSD}_{\text{C}\alpha} = 0.21 \text{ \AA}$  over 671 residues). C1 domain is also shown in cartoon representation. STX (red) is shown as space filling. Residues in the STX binding site are shown as sticks. (B) STX and derivatives. STX atom numbering is shown in italics. Dashed circles indicate sites of modification in STX derivatives. Gonyautoxin 5 is also known as ‘B1’.

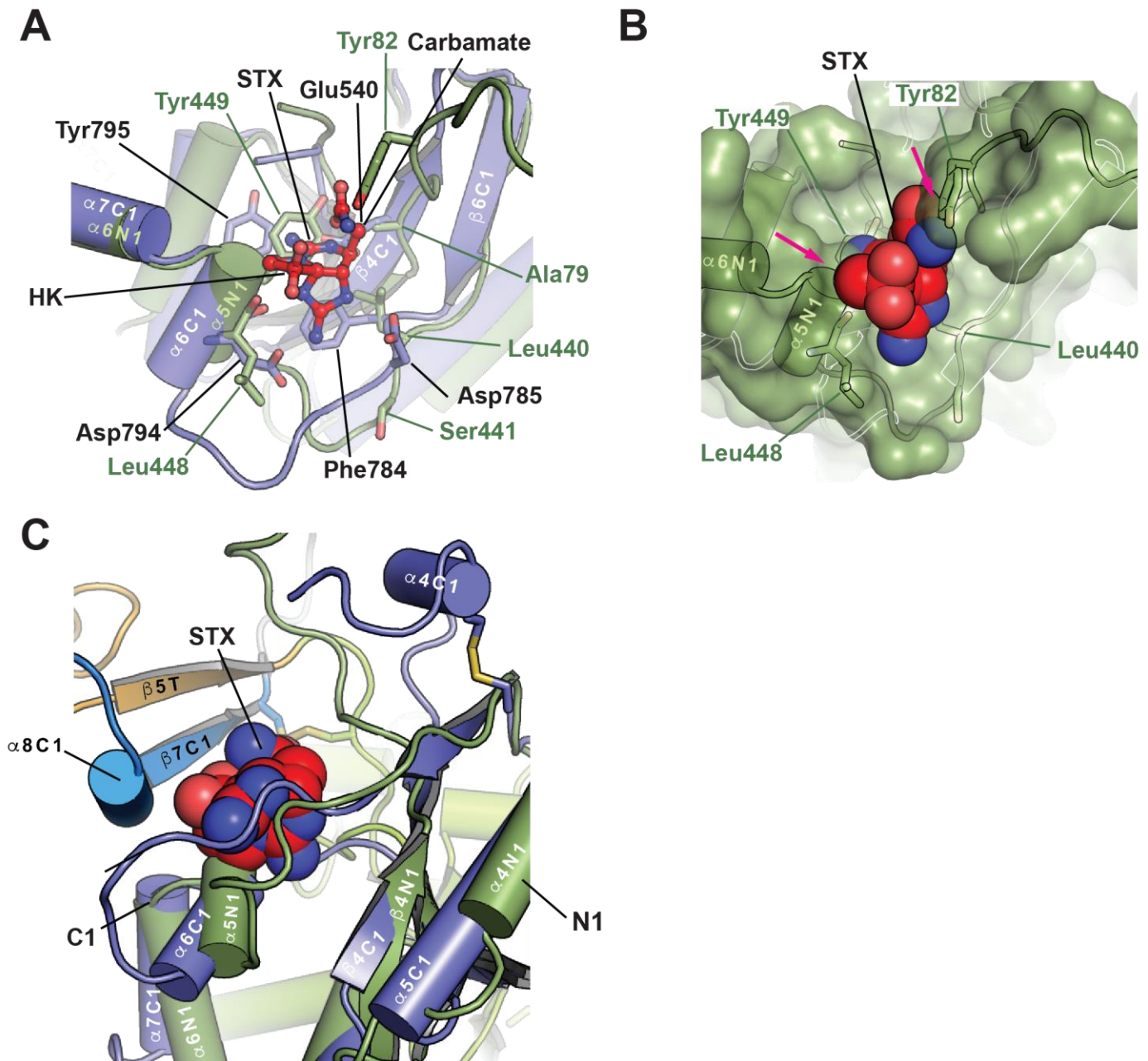


**Fig. S6. Structural comparison of Sxph N1 and C1 domains.** (A) Superposition of the Sxph N1 (green), and C1 (slate) domains ( $RMSD_{C\alpha} = 0.90 \text{ \AA}$  over 86 residues). STX is shown in red. N1 domain residues corresponding to C1 domain STX binding residues are shown as sticks and are labeled. (B) Surface rendering of the Sxph N1 proto-pocket (green). STX is shown in space-filling representation. Magenta arrows indicate clash sites. (C) Superposition Sxph N1 (green), and C1 (slate) domains. Elements from Sxph that occlude the N1 domain proto-pocket are labeled with black letters. STX (red) is shown in space filling representation.

Fig. S7

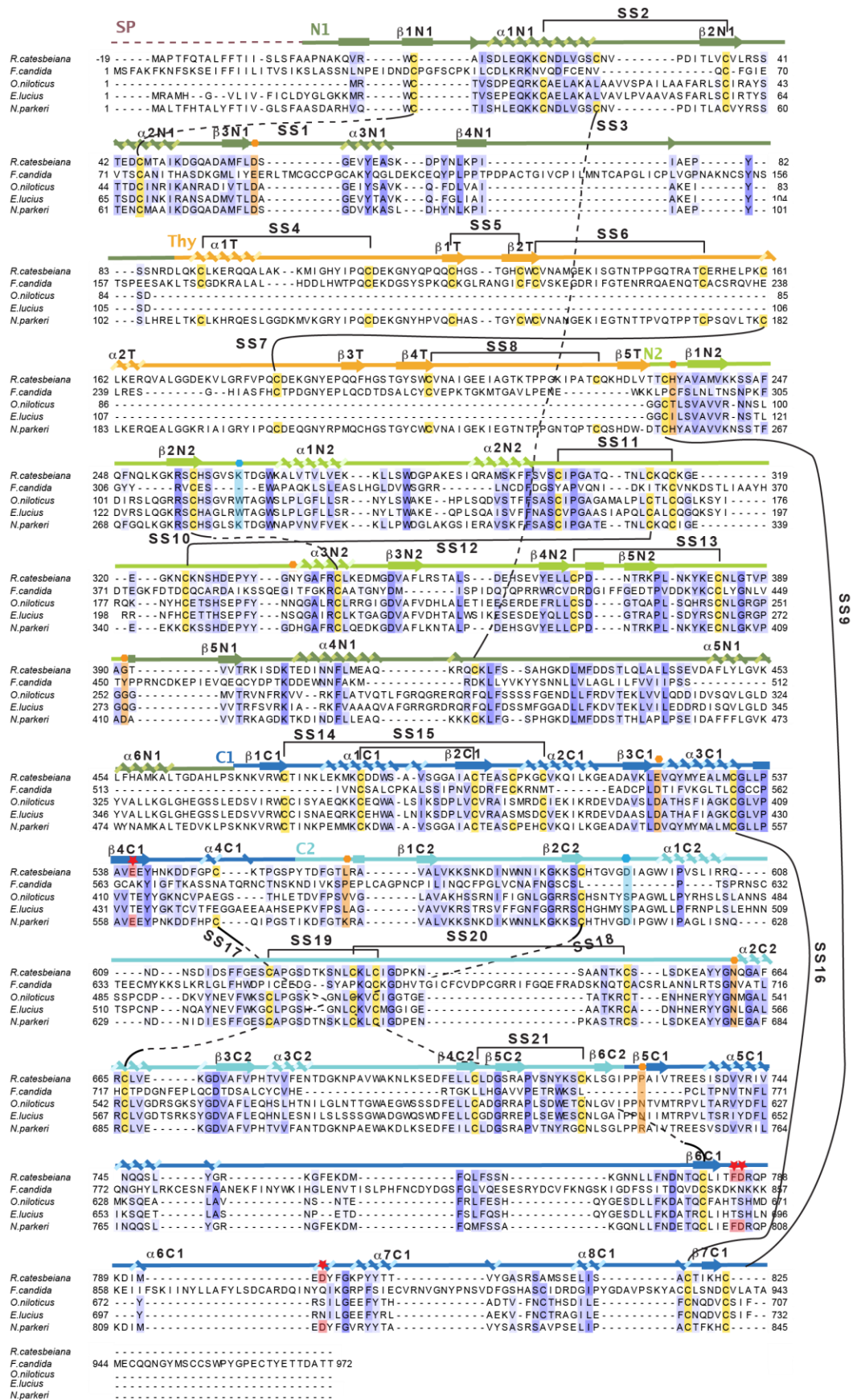


**Fig. S7. Sequence comparison of Sxph and putative Sxph homologs.** Sequence alignment of *Rana catesbeiana* Sxph with putative Sxph homologs from springtail (*Folsomia candida*) (NCBI: OXA56246.1), Nile tilapia (*Oreochromis niloticus*) (NCBI:XP\_019214738.1), Northern pike (*Esox lucius*) (NCBI:XP\_010879337.1), and High Himalaya frog (*Nanorana parkeri*) (NCBI: XP\_018410833.1).

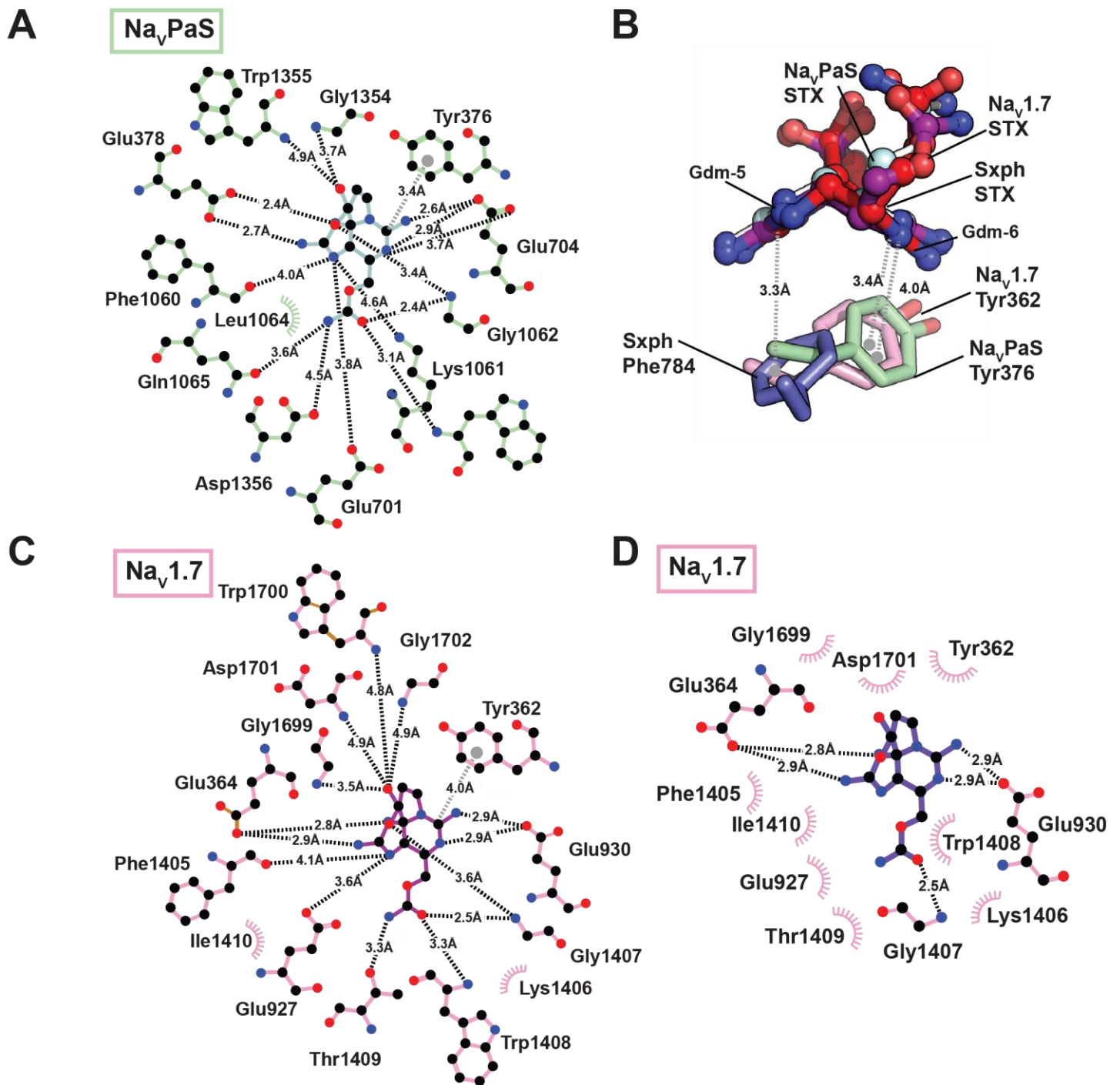


**Fig. S8. Na<sub>v</sub>PaS:STX and Na<sub>v</sub>1.7:STX interactions.** (A) Na<sub>v</sub>PaS:STX interactions (PDB 6a91)(29) determined with LIGPLOT (67) and a cutoff of 5.0 Å. (B) Comparison of STX cation- $\pi$  interactions with Sxph (blue), Na<sub>v</sub>PaS (green), and Na<sub>v</sub>1.7 (magenta). STX from the Sxph:STX complex (red), Na<sub>v</sub>PaS:STX complex (cyan), and Na<sub>v</sub>1.7:STX complex (violet) are indicated. (C and D) Na<sub>v</sub>1.7:STX

interactions (PDB:6J8G) (47) determined with LIGPLOT (67) a cutoffs of 5.0 Å and 3.35Å, respectively.

**Movie S1. Sxph conformational changes upon STX binding.** Morph between the apo-Sxph and Sxph:STX structures showing the STX binding pocket. Select sidechain and backbone atoms are shown as sticks. STX is shown as red sticks.